

The Interface of Coronene with Coinage Metals:
Geometric and Electronic Structure



Master Arbeit

Zur Erlangung des akademischen Grades eines
Master of Science
an der Naturwissenschaftlichen Fakultät der
Karl-Franzens-Universität Graz

vorgelegt von

Christian Simon Kern

Graz, 2018

Betreuer: Assoz.-Prof. Dr. Peter Puschnig

Abstract

In this work the metal-organic interface of the cyclic hydrocarbon molecule coronene ($C_{24}H_{12}$) adsorbed on three metal surfaces – Au(111), Ag(111) and Cu(111) – is studied with density functional theory.

As a first step, the most favorable adsorption sites of coronene on the three metal surfaces, as well as the optimal azimuthal orientation with respect to the substrate's high symmetry directions, are determined. After finding the optimal adsorption geometries for the different systems, we compare the results for adsorption heights and energies for different computational treatments of dispersive van der Waals-forces in the case of coronene on Au(111). Experimental data of benzene (C_6H_6) and hexa-peri-hexabenzocoronene ($C_{42}H_{18}$) serves as a reference to interpret the results obtained.

In the next step, we compare the electronic structure of the respective systems. For the case of Cu(111) simulations with a generalized-gradient- as well as a hybrid-functional for the exchange-correlation potential are presented.

With the one-step model of photoelectron emission, photoelectron angular distribution maps are simulated and discussed. In the case of coronene on Ag(111) we can directly compare these simulations to experimental results, for which we find good agreement.

Kurzzusammenfassung

In dieser Arbeit werden die metall-organischen Grenzflächen des zyklischen Kohlenwasserstoff-Moleküls Coronen, adsorbiert auf drei verschiedenen Metalloberflächen – Au(111), Ag(111) und Cu(111) – mittels Dichtefunktionaltheorie untersucht.

Im ersten Schritt werden die günstigsten Adsorptionsplätze von Coronen auf den drei Metalloberflächen, sowie die optimalen azimuthalen Drehrichtungen, bestimmt. Nachdem die optimale Adsorptionsgeometrie der verschiedenen Systeme gefunden wurde, vergleichen wir die Ergebnisse von Adsorptionshöhen und Energien für verschiedene numerische Methoden zur Behandlung der dispersiven Van-der-Waals Kräfte am Beispiel von Coronen auf Au(111). Experimentelle Daten von Benzen (C_6H_6) und Hexa-perihexabenzocoronene ($C_{42}H_{18}$) dienen zum Vergleich und der Interpretation der gewonnenen Ergebnisse.

Im nächsten Schritt vergleichen wir die elektronische Struktur der jeweiligen Systeme. Im Fall von Cu(111) werden Simulationen mit einem Generalized-gradient Funktional sowie mit einem Hybridfunktional präsentiert.

Mit dem *One-step Modell* der Photoelektronsemission werden winkelauflöste Verteilungskarten der Photoelektronsemission erzeugt und diskutiert. Für den Fall von Coronen auf Ag(111) können diese Simulationen, mit guter Übereinstimmung, unmittelbar mit experimentellen Daten verglichen werden.

Contents

1	Introduction	1
2	Methodology	5
2.1	The Theorem of Hohenberg and Kohn	5
2.2	The Kohn-Sham Scheme	9
2.3	Exchange-Correlation Functionals	11
2.3.1	Local Density Approximation	11
2.3.2	Generalized Gradient Approximation	12
2.3.3	Hybrid Functionals	12
2.4	Treatment of van der Waals-Forces	13
2.5	Computational Implementation	15
2.5.1	The Kohn-Sham Scheme in k-Space	15
2.5.2	The PAW Method	17
2.6	Photoemission Tomography	18
3	Results	19
3.1	Geometry Relaxations	19
3.1.1	Adsorption Geometry	19
3.1.2	Van der Waals Schemes	23
3.2	Electronic Structure	25
3.3	Photoemission Angular Distributions	29
4	Conclusions and Outlook	37

List of Abbreviations

ACFDT	adiabatic-connection and fluctuation-dissipation theorem
APW	augmented plane-wave
BZ	Brillouin zone
DFT	density functional theory
DOS	density of states
fcc	face-centered cubic
FFT	fast Fourier transformation
GGA	generalized gradient approximation
HBC	hexa-peri-hexabenzocoronene
HO	harmonic oscillator
HSE	Heyd-Scuseria-Ernzerhof
LAPW	linearized augmented plane-wave
LDA	local density approximation
LEED	low-energy electron diffraction
MBD	many body dispersion
ML	monolayer
OFET	organic field effect transistors
OLED	organic light emitting diode
OPW	orthogonalized plane-wave
PAW	projector augmented wave
PBE	Perdew-Burke-Ernzerhof

pDOS	projected density of states
PTCDA	perylene-tetracarboxylic dianhydride
PT	photoemission tomography
QMC	quantum Monte Carlo
RPA	random phase approximation
SE	Schrödinger equation
TC-SCS	Tkatchenko-Scheffler with self-consistent screening
TS	Tkatchenko-Scheffler
UPS	ultra-violet photoemission spectroscopy
VASP	Vienna Ab-initio Simulation Package
vdWf	van der Waals-force

List of Figures

3.1	Adsorption sites for the center of the coronene molecules on the (111)-surface, denoted from left to right: center, top, bridge. . .	20
3.2	Optimized adsorption sites of coronene on Ag(111) (left) and coronene on Cu(111) (right). The rotational angle ϕ is defined as the positive rotation between the zig-zag-orientation of the molecule and the fcc $[\bar{1}10]$ -direction.	21
3.3	Total energies of coronene on the (111)-surfaces of gold, silver and copper with respect to the rotational angle of the molecule. The angle of 0° is defined such that the zig-zag orientation of coronene is in the $[\bar{1}10]$ -direction of the substrate. Rotations further than 30° are redundant because of the molecule's symmetry. The calculations were done with the PBE exchange-correlation functional and the TS van der Waals-correction with optimized parameters.	22
3.4	DOS of the composite systems of coronene on the adsorbates Au(111), Ag(111) and Cu(111) respectively.	25
3.5	The pDOS of the interface coronene-Au(111) in the upper panel and of coronene-Ag(111) in the lower panel.	26
3.6	The pDOS of the interface coronene-Cu(111). Upper panel: evaluated with the GGA functional. Lower panel: evaluated with the HSE functional.	27
3.7	From left to right: coronene on Au(111), Ag(111) and Au(111). From top to bottom: $\Delta E_{\text{pot}}(z)$ with $\Delta\Phi$ indicating the change in work function, $Q(z)$ and $\Delta\rho(z)$. The charge-densities of the substrate (in the respective color) and those of the molecule (brown) have been added in dashed lines to indicate atomic positions (arb. units, scaled in magnitude).	32
3.8	Photoemission angular distribution maps of 1 ML of free-standing coronene. Left and middle show the two degenerate states that form the HOMO (right). The k -space is measured in units of \AA^{-1} , the photoemission intensity has been normalized to 1. . .	33

- 3.9 Photoemission angular distribution maps of the HOMO emission. Left is the map of 1 ML of coronene (symmetrized for comparison), in the middle coronene on Au(111) and to the right coronene on Ag(111). The k -space is measured in units of \AA^{-1} , the photoemission intensity has been normalized to 1. . . 33
- 3.10 Upper panel: theoretical results for coronene on Ag(111) with the HOMO feature in the middle and binding energies of ± 0.1 eV with respect to the HOMO to the left and right. Lower panel: zoom-in of the theoretical calculations (top) compared to experimental results (bottom) respective to the above energies. . . 34
- 3.11 Photoemission angular distribution maps of coronene on Cu(111). Left and middle panels show the maps calculated with the PBE functional at the binding energies of -1.6 eV and -2.4 eV respectively. To the right the HOMO feature calculated with the HSE functional is shown. Note that the in the latter – due to computational limitations that do not allow for a finer k -space mesh with the HSE functional – a broadening in k -space $\Delta k = 0.1 \text{\AA}^{-1}$ was used instead of $\Delta k = 0.05 \text{\AA}^{-1}$. The k -space is measured in units of \AA^{-1} , the photoemission intensity has been normalized to 1. 35

List of Tables

3.1	Total energies of different adsorption sites of coronene on Au(111), Ag(111) and Cu(111) computed with the PBE exchange-correlation functional and TS method for van der Waals-corrections with optimized parameters (most favorable ones highlighted).	20
3.2	Adsorption energies and adsorption heights of coronene on Au(111), Ag(111) and Cu(111) at optimized sites.	23
3.3	Adsorption energies and adsorption heights of coronene on Au(111) for the PBE functional with different van der Waals-correction schemes: Tkatchenko-Scheffler (TS), TS with self-consistent screening (TS-SCS), many-body dispersion (MBD) and MBD with SCS.	24

Chapter 1

Introduction

The field of organic semiconductors research, and with it the description of metal-organic interfaces, has been active for the past 30 years and is ever growing to this date. Numerous possibilities for the actual fabrication of organic electronics and opto-electronics are being developed and some have already been put on the market, such as organic light emitting diodes (OLED), organic field effect transistors (OFET) or polymer photovoltaics.

With metal-organic interfaces, electronic and opto-electronic properties can be tuned in an almost unlimited scope, which also explains the great success of these systems. Among the properties that can be tailored are energy levels, gap sizes, light adsorption- and emission spectra, inter-molecular interactions, the properties of charge carrier transport and moreover the actual determinants of the manufacturing process. The main reasons for this diversity come along with the electronic structure: aromatic hydrocarbon molecules have delocalized π -electrons which are responsible for their exceptional electronic and optical intra-molecular properties [1]. However, the question of charge transport between adjacent molecules in thin films of heterostructures is more involved than with classical semiconductors and charge injection from the metal into the organic is determined by the level alignment of the interface. Moreover, the absence of strong intermolecular forces and the weak binding to metal surfaces in the van der Waals-regime has consequences that makes it necessary to put considerable effort in the understanding of organic molecules on metal surfaces. In this thesis we study such a system, namely the adsorption of coronene on the surfaces of gold, silver and copper.

The molecule coronene ($C_{24}H_{12}$), an organic, π -conjugated molecule consisting of 6 benzene rings grouped flatly around another one in the center, is such a molecule. It occurs naturally in the mineral carpathite and shows fluorescence under ultra-violet light when in solution [2]. Potassium-doped coronene crystals have gained particular interest for showing superconductive behavior up to 15 K [3]. The three fcc (111)-surfaces of gold, silver and copper

– as a group often referred to as the *Coinage metals* – are typical noble metal surfaces to deposit organic materials on and can serve as electrodes in organic semiconductor structures.

The course of this work is outlined as follows. In the next chapter the theoretical framework of the method being used, is introduced. After the foundations of density functional theory (DFT) have been laid, the techniques and approximations necessary to compute many-particle systems are depicted. Here the focus is put on the approximations for three different exchange-correlation functionals as well as three different treatments of van der Waals-forces. After this comparison follows a short introduction to the DFT code being used in this thesis, i.e. the Vienna Ab-initio Simulation Package (VASP). The theoretical part of this thesis is then concluded with a summary about the simulation of photoemission spectroscopy, which is described within the one-step model of photoelectron emission.

The remaining chapter is devoted to the results obtained within this thesis. As a first step, the optimal adsorption geometry of coronene on each of the three metal surfaces is determined. We first find the most favorable adsorption site on each metal surface and then the optimal azimuthal orientation of the molecule with respect to the surface. When determining the adsorption height and energy, particular emphasis is laid on the interface coronene/Au(111), for which three different van der Waals-correction schemes are compared. In lack of experimental data for this system, we compare the results to the adsorption of benzene (C_6H_6) on Au(111) and hexa-peri-hexabenzocoronene ($C_{42}H_{18}$) on the same surface.

In order to examine the electronic structure of the three respective systems, the density of states is presented, where, in the case of Cu(111), a more sophisticated calculation with a hybrid functional is added to bridle shortcomings of the functional used otherwise. The most interesting physics of a metal-organic interface happens at the gap between the metal surface and the molecule. Here we show the behavior of the difference in charge density and its derivatives with respect to the z -direction as well as the change in work function. Although we do not see any major charge transfer for these systems, the reduction of the work function caused by the Pauli push-back effect of the spill-out electron charge of the metal is visible.

The power and the success of the method of *Orbital Tomography* lies not only in the experimental improvements that made it possible to reconstruct maps of molecular orbitals and surfaces from photoelectron spectroscopy, but also in the fact that we have a simple model at hand that allows the experimental data to be compared with DFT results. The 2D \mathbf{k} -space maps of the most important molecular orbital of coronene, the highest occupied molecular orbital (HOMO), are compared to those of the HOMO feature of the adsorbed layers. Accordingly, the change in electronic structure due to

the inter-molecular interaction and the molecule-substrate interaction is made visible and can be quantified to some extent.

For the case of coronene on Ag(111), this HOMO emission is compared to an experimental result that was published in 2017 alongside with some of the results of this thesis [\[4\]](#).

Chapter 2

Methodology

In this chapter the theoretical foundations of methods used in this work are laid. A short introduction to density functional theory (DFT) is given, where the emphasis is on how VASP incorporates the concepts of DFT. In this course, the main focus is on the computational treatment of van der Waals-interactions, conceptually leaning towards the application in the field of metal-organic interfaces.

2.1 The Theorem of Hohenberg and Kohn

If one wants to treat a condensed matter system on a non-relativistic quantum mechanical footing, the Hamiltonian of the system will consist of contributions from the protons, the electrons and the interaction between both. For such a many-body system, the cores are usually treated as a slowly varying background which generate a potential for the fast moving electrons, i.e. the *Born-Oppenheimer approximation* [5]. The Hamiltonian for the electron system can now be written in the form

$$\hat{H} = \hat{T} + \hat{V} + \hat{U}. \quad (2.1)$$

\hat{T} is the kinetic energy operator of the electrons, \hat{V} the single-particle potential operator (i.e. Coulomb attraction from the cores or external fields) and \hat{U} the interaction potential operator (i.e. Coulomb repulsion between electrons). To distinguish between formal operators and their spatial representation, we will denote the latter with lower-case letters. In the language of second quantization [6, 7] and measured in natural units ($\hbar = m_e = e = 1$), these integrals read

$$\begin{aligned} \hat{H} = & -\frac{1}{2} \int d^3\mathbf{r} \hat{\psi}_\sigma^\dagger(\mathbf{r}) \nabla^2 \hat{\psi}_\sigma(\mathbf{r}) + \int d^3\mathbf{r} \hat{\psi}_\sigma^\dagger(\mathbf{r}) V(\mathbf{r}) \hat{\psi}_\sigma(\mathbf{r}) \\ & + \frac{1}{2} \int d^3\mathbf{r} \int d^3\mathbf{r}' \hat{\psi}_\sigma^\dagger(\mathbf{r}) \hat{\psi}_{\sigma'}^\dagger(\mathbf{r}') U(\mathbf{r}, \mathbf{r}') \hat{\psi}_{\sigma'}(\mathbf{r}') \hat{\psi}_\sigma(\mathbf{r}), \end{aligned} \quad (2.2)$$

where implicit summation over spin variables σ and σ' is understood. The field operator $\hat{\psi}_\sigma^\dagger(\mathbf{r})$ creates an electron with spin σ at the site \mathbf{r} , which can be expressed in terms of creation- and annihilation-operators and a suitable one-particle basis set $\{\varphi_i(\mathbf{r})\}$:

$$\hat{\psi}^{(\dagger)}(\mathbf{r}) = \sum_i \varphi_i(\mathbf{r}) a_i^{(\dagger)}. \quad (2.3)$$

For the following, we will oppress the spin index and assume intrinsic summation over spin indices. The fermionic character of the system is reflected in the algebra of the creation- and annihilation-operators ($\{a_i, a_j^\dagger\} = \delta_{ij}$ plus trivial ones). These operators act on the *Fock* vacuum state $|0\rangle$ (with suitable normalization etc.) to create an N -particle state $|\Psi\rangle$, which is in turn a solution to the stationary Schrödinger equation (SE)

$$\hat{H} |\Psi\rangle = (\hat{T} + \hat{V} + \hat{U}) |\Psi\rangle = E |\Psi\rangle. \quad (2.4)$$

We now assume that the ground state of this system is non-degenerate and has the solution Ψ_0 , i.e.

$$\hat{H} |\Psi_0\rangle = E_0 |\Psi_0\rangle. \quad (2.5)$$

The only part in the Hamiltonian that is unique for each system is \hat{V} , because the kinetic term and the interaction terms are entirely governed by electron properties that do not differ to the electron gas. Consequently, there exists a set of potentials \mathcal{V} that have a set of ground-state solutions Ψ_0 such that a surjective mapping exists.

$$\mathcal{M}_1 : \mathcal{V} \rightarrow \Psi_0 \quad (2.6)$$

The set of ground state densities \mathcal{N} for the corresponding wave-function consists of all elements $n(\mathbf{r})$:

$$n(\mathbf{r}) = \langle \Psi_0 | \hat{\psi}^\dagger(\mathbf{r}) \hat{\psi}(\mathbf{r}) | \Psi_0 \rangle, \quad \forall |\Psi_0\rangle \in \Psi_0. \quad (2.7)$$

Therefore, another surjective mapping exists, that maps the ground states to the densities, i.e.

$$\mathcal{M}_2 : \Psi_0 \rightarrow \mathcal{N}. \quad (2.8)$$

If the two surjective mappings, \mathcal{M}_1 and \mathcal{M}_2 , are each one-to-one (injective), we can fully invert the combined mapping (bijective) $\mathcal{M} = \mathcal{M}_2 \circ \mathcal{M}_1$:

$$\mathcal{M}^{-1} = (\mathcal{M}_2 \circ \mathcal{M}_1)^{-1}. \quad (2.9)$$

The first task on the agenda is now to show that \mathcal{M}_1 is injective, i.e. showing that two potentials

$$\hat{V}, \hat{V}' \in \mathcal{V} : \hat{V} \neq \hat{V}' + \text{const.} \quad (2.10)$$

lead to different ground state solutions $|\Psi_0\rangle, |\Psi'_0\rangle \in \Psi_0$ in the SEs:

$$\begin{aligned} (\hat{T} + \hat{V} + \hat{U})|\Psi_0\rangle &= E_0 |\Psi_0\rangle, \\ (\hat{T} + \hat{V}' + \hat{U})|\Psi'_0\rangle &= E'_0 |\Psi'_0\rangle. \end{aligned} \quad (2.11)$$

Assuming the contrary that we want to prove, $|\Psi_0\rangle = |\Psi'_0\rangle$, and subtracting the two SEs from each other, we get

$$(\hat{V} - \hat{V}')|\Psi_0\rangle = (E_0 - E'_0)|\Psi_0\rangle, \quad (2.12)$$

which leads to a contradiction to the assumption 2.10, not unless if the wave functions would vanish on the whole domain, which is rather unphysical. We have just proven that \mathcal{M}_1 is indeed one-to-one and will now continue to do the same for \mathcal{M}_2 , i.e. we want to show that

$$|\Psi_0\rangle \neq |\Psi'_0\rangle \Rightarrow n(\mathbf{r}) \neq n'(\mathbf{r}). \quad (2.13)$$

From the variational principle of *Rayleigh-Ritz*¹ it follows that on the one hand

$$\begin{aligned} E_0 = \langle \Psi_0 | \hat{H} | \Psi_0 \rangle &< \langle \Psi'_0 | \hat{H} | \Psi'_0 \rangle = \langle \Psi'_0 | (\hat{H}' + \hat{V} - \hat{V}') | \Psi'_0 \rangle = \\ &E'_0 + \int d^3\mathbf{r} n'(\mathbf{r})[V(\mathbf{r}) - V'(\mathbf{r})], \end{aligned} \quad (2.14)$$

and on the other hand

$$E'_0 < E_0 + \int d^3\mathbf{r} n(\mathbf{r})[V'(\mathbf{r}) - V(\mathbf{r})]. \quad (2.15)$$

Again, we assume the contrary of what we want to prove, $n(\mathbf{r}) = n'(\mathbf{r})$, and add 2.14 to 2.15, only to find that this results in the contradiction

$$E_0 + E'_0 < E_0 + E'_0. \quad (2.16)$$

In *reductio ad absurdum*, we have seen that both \mathcal{M}_1 and \mathcal{M}_2 are bijective, from which follows that \mathcal{M} is a fully invertible one-to-one mapping. Consequently, we have established the first result of the famous 1964 paper by Hohenberg and Kohn [9]: the ground-state density uniquely determines (up to a constant) the local external potential $v(\mathbf{r})$ that gives rise to it.² Furthermore, any observable \hat{O} can be expressed as a functional of the ground-state density $n(\mathbf{r})$:

$$\hat{O}[n] = \langle \Psi_0[n] | \hat{O} | \Psi_0[n] \rangle, \quad (2.17)$$

which reads for the energy in particular

$$E[n] = \langle \Psi_0[n] | (\hat{T} + \hat{U} + \hat{V}) | \Psi_0[n] \rangle. \quad (2.18)$$

¹see e.g. [8], Vol. II p. 330 ff.

² [10], p.332

This energy is the true ground-state energy if, and only if, the density is the ground-state density, E_0 can therefore be obtained via a minimization process:

$$E_0 = \min_{n \in \mathcal{N}} E[n]. \quad (2.19)$$

In order to establish more terminology, we define the universal functional, or sometimes called the Hohenberg-Kohn functional, as

$$F[n] = \langle \Psi_0[n] | (\hat{T} + \hat{U}) | \Psi_0[n] \rangle, \quad (2.20)$$

in order to rewrite 2.18 as

$$E[n] = F[n] + \int d^3\mathbf{r} V(\mathbf{r})n(\mathbf{r}), \quad (2.21)$$

which again emphasizes the fact that $F[n]$ is independent of the local potential, i.e. independent of the system.

From the perspective of variational calculus, the minimum condition 2.19 might also be formulated in another way: the energy is stationary if small variations around the ground-state energy vanish, i.e. $\delta E = 0$. Using the functional derivative of $F[n]$, $\delta F[n]/\delta n(\mathbf{r})$, we can write the variation of the energy functional as

$$E[n + \eta\delta n] - E[n] = \eta \int d^3\mathbf{r} \left[\frac{\delta F[n]}{\delta n(\mathbf{r})} + V(\mathbf{r}) \right] \delta n(\mathbf{r}) + \mathcal{O}(\eta^2) \stackrel{!}{=} 0, \quad (2.22)$$

where η is a small positive parameter and $\delta n(\mathbf{r})$ the variation of the density. The latter must lead to densities that still have the same total particle number, thus the variation is restricted but still arbitrary enough such that 2.22 can only hold, up to order of η , if the term in brackets vanishes, which leads to the condition

$$\frac{\delta F[n]}{\delta n(\mathbf{r})} = -V(\mathbf{r}). \quad (2.23)$$

Using the density as the main variable to describe an N -electron system, has brought us from a wave-function based description with $3N$ parameters, to a density based description with 3 parameters, which is an enormous simplification in terms of computational effort when it comes to systems with realistic sizes. Several subtleties have been left out in the discussion above, such as the possibility of a degenerate ground-state, a thorough examination for which class of densities and potentials the proof holds and the extension to e.g. spin-polarized systems, excited states or finite temperature [11, 10, 12, 13]. The question how the minimization process of 2.19 can be done and how to calculate observables will be subject to the next sections.

2.2 The Kohn-Sham Scheme

The idea that flattened the path for the success of DFT came from Kohn and Sham in 1965 [14] and drew its logic from the following argument: for each interacting N -electron system, for which the knowledge of its ground-state density is sufficient to describe all physical observables, there exists a corresponding non-interacting N -electron system that has the same ground-state density. For this auxiliary system, one can also formulate an energy functional according to the theorem of Hohenberg and Kohn, the only difference here is, of course, the lacking of the interaction term:

$$E_a[n_a] = T_a[n_a] + \int d^3\mathbf{r} V_a(\mathbf{r})n_a(\mathbf{r}). \quad (2.24)$$

The variation of the energy with respect to the density (under the constraint that the density is positive definite and conserves the particle number), $\delta E_a[n] = 0$, gives the ground-state density which shall be equal to that of the interacting system, i.e.

$$n_a(\mathbf{r}) = n(\mathbf{r}). \quad (2.25)$$

If the ground-state is again non-degenerate, both densities can be represented in a one-particle basis that are solutions of the one-particle effective SE

$$\left(-\frac{1}{2}\nabla^2 + v_a(\mathbf{r})\right)\phi_i(\mathbf{r}) = \epsilon_i\phi_i(\mathbf{r}) \Rightarrow n(\mathbf{r}) = \sum_i |\phi_i(\mathbf{r})|^2. \quad (2.26)$$

For the actual interacting system, we have the original energy functional as

$$E[n] = T[n] + U[n] + \int d^3\mathbf{r} V(\mathbf{r})n(\mathbf{r}), \quad (2.27)$$

to which we will now add and subtract the kinetic energy functional of the non-interacting system, T_a , and the classical electron-electron repulsion, i.e. the Hartree energy-functional

$$E_H[n] = \frac{1}{2} \int d^3\mathbf{r} \int d^3\mathbf{r}' \frac{n(\mathbf{r})n(\mathbf{r}')}{|\mathbf{r} - \mathbf{r}'|}, \quad (2.28)$$

such that the energy functional reads

$$E[n] = T[n] + T_a[n] - T_a[n] + E_H[n] - E_H[n] + U[n] + \int d^3\mathbf{r} V(\mathbf{r})n(\mathbf{r}). \quad (2.29)$$

In doing so, we can introduce the *exchange-correlation* energy functional $E_{xc}[n]$ as

$$E_{xc}[n] = T[n] + U[n] - T_a[n] - E_H[n] = F[n] - T_a[n] - E_H[n], \quad (2.30)$$

and rewrite the energy functional as

$$E[n] = T_a[n] + E_H[n] + E_{xc}[n] + \int d^3\mathbf{r} V(\mathbf{r})n(\mathbf{r}). \quad (2.31)$$

We can now vary the density in the same fashion as in 2.22 to obtain a minimum for the energy:

$$0 \stackrel{!}{=} E[n + \eta\delta n] - E[n] = \eta \int d^3\mathbf{r} \left[\frac{\delta T_a}{\delta n(\mathbf{r})} + \int d^3\mathbf{r}' \frac{n(\mathbf{r}')}{|\mathbf{r} - \mathbf{r}'|} + \frac{\delta E_{xc}}{\delta n(\mathbf{r})} + V(\mathbf{r}) \right] \delta n(\mathbf{r}) + \mathcal{O}(\eta^2). \quad (2.32)$$

As above, the integral vanishes always if the term in brackets vanishes. This leads to the condition

$$\frac{\delta T_a}{\delta n(\mathbf{r})} = -V_H(\mathbf{r}) - V_{xc}(\mathbf{r}) - V(\mathbf{r}) \equiv -V_{KS}(\mathbf{r}), \quad (2.33)$$

where we have introduced the resulting effective potential, the *Kohn-Sham potential* $V_{KS}(\mathbf{r})$, and have used

$$\frac{\delta E_H[n]}{\delta n(\mathbf{r})} = \int d^3\mathbf{r}' \frac{n(\mathbf{r}')}{|\mathbf{r} - \mathbf{r}'|} \equiv V_H(\mathbf{r}) \quad \text{and} \quad \frac{\delta E_{xc}}{\delta n(\mathbf{r})} \equiv V_{xc}(\mathbf{r}). \quad (2.34)$$

The Kohn-Sham potential is a local potential (although it functionally depends on non-local entities) and instead of minimizing the energy functional, it is equivalent to solve the Schrödinger system of non-interacting electrons in an effective Kohn-Sham potential, which is referred to as the *Kohn-Sham equation*:

$$\left[-\frac{1}{2}\nabla^2 + V_{KS}(\mathbf{r}) \right] \phi_i(\mathbf{r}) = \varepsilon_i \phi_i(\mathbf{r}). \quad (2.35)$$

Since the form of the Kohn-Sham potential is unknown, one has to solve the above equation self-consistently:

1. start with an initial guess of N orbitals
2. construct the density via $n(\mathbf{r}) = \sum_i^N |\phi_i(\mathbf{r})|^2$ and with it the potential
3. solve the Kohn-Sham equation with a chosen approximation for the exchange-correlation functional
4. reconstruct the density and compare to initial density
5. repeat 2.–5. until desired convergence is reached

Once the self-consistent density has been obtained, the ground state energy can be constructed in the following way. The non-interacting kinetic energy functional for the ground-state density is constructed as

$$T_a[n] = \sum_i^N \varepsilon_i - \int d^3\mathbf{r} V_{\text{KS}}(\mathbf{r})n(\mathbf{r}), \quad (2.36)$$

which we can now insert in the expression for the energy functional of the interacting system (eq. 2.21) and use eq. 2.30 to get the final expression for the ground-state energy:

$$E[n] = \sum_i^N \varepsilon_i - \int d^3\mathbf{r} n(\mathbf{r}) \left[\frac{1}{2} \int d^3\mathbf{r}' \frac{n(\mathbf{r}')}{|\mathbf{r} - \mathbf{r}'|} + V_{\text{xc}}(\mathbf{r}) \right] + E_{\text{xc}}[n]. \quad (2.37)$$

It is important to emphasize that this ground-state energy is in principle exact, although in practice the exchange-correlation functional has to be approximated. The Kohn-Sham orbitals however, do not represent the true ground-state wave function but can rather be seen as an approximation.³ The main difficulty in practical DFT calculations lies in the construction of the exchange-correlation functional, a topic that will be briefly touched in the next section.

2.3 Exchange-Correlation Functionals

For the treatment of exchange and correlation effects, as well as kinetic energy effects that lie beyond the non-interaction approximation $T_a[n]$ of the last section, we want a functional that is both computationally efficient and describes all these effects with the most desirable precision. Since $E_{\text{xc}}[n]$ must be constructed from the densities in the iterative calculation scheme, an explicit functional dependence on $n(\mathbf{r})$ is necessary.

For the construction of these functionals two approaches are possible. On the one hand, one can improve the accuracy in the description of physical systems by means of fitting parameters to the actual systems as an *empirical* method. On the other hand, one can construct functionals from pure theory, which is called *ab-initio*, although parameters are used, but they are not fitted to the experiment. While empirical methods are of widespread use in chemistry and applied physics, we restrict ourselves to an ab-initio approach in this work.

2.3.1 Local Density Approximation

The simplest yet very successful approximation, the local density approximation (LDA), takes the exchange-correlation energy per particle of the homogeneous electron gas at a certain density, $\epsilon_{\text{xc}}(n)$. The exchange part of this entity

³The N -th eigenvalue can be seen as an exception. It could be shown that $-\varepsilon_N$ is the first ionization energy for the N -electron system, see e.g. [15] p. 35 ff and references therein.

is known exactly, whereas the correlation part is simulated by e.g. Quantum Monte Carlo (QMC) methods.

$$E_{\text{xc}}^{\text{LDA}}[n] = \int d^3\mathbf{r} n(\mathbf{r}) \epsilon_{\text{xc}}(n(\mathbf{r})). \quad (2.38)$$

In principle, such an approximation is only valid for a very slow varying density. Nonetheless, this scheme has also been successfully applied to a wide range of systems without such restrictions. The great success of the LDA is partly owed to the fact that errors in the exchange treatment cancel those of the correlation on a systematic level [16].

2.3.2 Generalized Gradient Approximation

Extending the LDA, it would be desired to not only consider the density at point \mathbf{r} but also its changes at that point to account for spatially rapidly varying situations. Approximations that take the densities and their gradients into account are called generalized gradient approximations (GGAs)[17] and are of the general form

$$E_{\text{xc}}^{\text{GGA}}[n] = \int d^3\mathbf{r} f(n(\mathbf{r}), \nabla n(\mathbf{r})). \quad (2.39)$$

A successful implementation of this kind is the Perdew-Burke-Ernzerhof (PBE) functional, which was also used in the practical calculations of this work. A class of functionals that use the density, its gradient and also the (non-interacting) kinetic energy density,

$$n_{\text{T}}(\mathbf{r}) = \frac{1}{2} \sum_i^N |\nabla \varphi_i(\mathbf{r})|^2, \quad (2.40)$$

are referred to as *meta-GGA* functionals:

$$E_{\text{xc}}^{\text{M-GGA}}[n] = \int d^3\mathbf{r} f(n(\mathbf{r}), \nabla n(\mathbf{r}), n_{\text{T}}(\mathbf{r})). \quad (2.41)$$

The performance of meta-GGA is reported to be superior to plain GGA for most systems, since the additional entity $n_{\text{T}}(\mathbf{r})$ can fulfill more constraints, e.g. the correlation energy is self-interaction free [18].

2.3.3 Hybrid Functionals

A class of functionals that takes local- and semilocal approximations and additionally exact exchange into account, are the hybrid functionals. Exact exchange from Hartree Fock theory is non-local due to the pairwise interaction of all electrons [19]:

$$E_{\text{x}}^{\text{HF}} = -\frac{1}{2} \sum_{i,j}^N \int d^3\mathbf{r} \int d^3\mathbf{r}' \frac{\varphi_i(\mathbf{r})\varphi_j(\mathbf{r}')\varphi_j(\mathbf{r})\varphi_i(\mathbf{r}')}{|\mathbf{r} - \mathbf{r}'|}. \quad (2.42)$$

Hybrid functionals mix the different kinds of interactions, usually regulated by a mixing parameter. In the case of range-separated hybrid functionals, the amount of contributions from semi-local exchange-correlation functionals and exact exchange is dependent on the distance, resulting in different behavior for the long-range and the short-range interactions [20]. The improved accuracy of this scheme is paid with a steep increase of computational effort, therefore such a calculation is usually done as a second step after geometry relaxation of the system has been computed with a local or semi-local functional. Here we have used the Heyd-Scuseria-Ernzerhof (HSE) functional [21, 22, 23].

2.4 Treatment of van der Waals-Forces

One part of the correlations between electrons are long-range dispersion interactions referred to as van der Waals-forces (vdWFs). These forces arise from spontaneous fluctuations in the density of one atom, molecule or surface, resulting in electric fields that can induce a polarization of other, remote constituents of the system. In the dipole approximation, the energy between two atoms with electric polarizabilities α_1 and α_2 scales with

$$E_{\text{vdWF}}^{\text{dipole}} \propto -\frac{\alpha_1\alpha_2}{|\mathbf{r}_1 - \mathbf{r}_2|^6}, \quad (2.43)$$

thus an attractive, long-range force results that is not incorporated in local or semi-local correlation functionals. There are several ways to incorporate these effects at different levels of sophistication [24]. A functional that is explicitly designed for these purposes, treats the non-local part of the correlation energy from vdWF as

$$E_c^{\text{nl}} = \int d^3\mathbf{r} \int d^3\mathbf{r}' n(\mathbf{r})\Xi(\mathbf{r}, \mathbf{r}')n(\mathbf{r}'), \quad (2.44)$$

where the integral kernel $\Xi(\mathbf{r}, \mathbf{r}')$ is a function of the spatial separation $|\mathbf{r} - \mathbf{r}'|$ and a functional of the respective densities and their gradients [25].

In this work however, we use a different approach for vdWFs and treat these interactions as corrections to the ground-state energy that are computed as an additional step after the Kohn-Sham scheme. In order to compare different levels of these corrections, we have used different methods, the standard being the Tkatchenko-Scheffler (TS) method [26]. Here, only the pairwise interaction between different atoms is described as

$$E_{\text{vdWF}} = -\frac{1}{2} \sum_{i,j} f_{\text{damp}}(|\mathbf{r}_i - \mathbf{r}_j|, \mathbf{R}_i^0, \mathbf{R}_j^0) \frac{C_{ij}^6}{|\mathbf{r}_i - \mathbf{r}_j|^6}, \quad (2.45)$$

with the major ingredient being the C_{ij}^6 coefficients that should represent the polarizability of each atom and that are computed beforehand, either from

model systems or fitted to experiments. The function f_{damp} is needed to switch off vdWFs at short distances, in which the \mathbf{R}_i^0 play the role of short-range cutoff-parameters. We use C_{ij}^6 , \mathbf{R}_i^0 and atomic polarizabilities α_i that are designed to describe organic-metal-interfaces more accurately than those of the original TS method [27].

One of the most apparent shortcomings of the TS method is the lacking of screening effects. Since each atom of a molecule or a surface has a dipole field and is itself polarizable, screening plays an important role, especially when other dipole fields lie in between long-range interactions, i.e. intermediate atoms screen the electric fields. Such effects have to be treated on a many-body level, it is however possible to use a two-body approximation when the atomic polarizability is not taken as an external parameter α_i for each atom, but taken to be frequency-dependent and continuous in space: $\alpha(\mathbf{r}, i\omega)$. Moreover, the polarizabilities are interacting in the sense that they feel a first-order dipole correction via the field-tensor $\Theta(\mathbf{r}, \mathbf{r}')$ to the $\alpha_i^{\text{TS}}(\mathbf{r}, i\omega)$, such that

$$\alpha^{\text{SCS}}(\mathbf{r}, i\omega) = \alpha_i^{\text{TS}}(\mathbf{r}, i\omega) + \alpha^{\text{TS}}(\mathbf{r}, i\omega) \int d^3\mathbf{r}' \Theta(\mathbf{r}, \mathbf{r}') \alpha^{\text{SCS}}(\mathbf{r}, i\omega). \quad (2.46)$$

This integral-equation has to be solved self-consistently to get correct polarizabilities for each frequency $i\omega$ at each point in space \mathbf{r} [28]. In practice, the $\alpha_i^{\text{TS}}(\mathbf{r}, i\omega)$ are taken to be frequency-dependent only and are given a certain value at each atom site i . We are thus replacing the integration over space by summation over all other atoms:

$$\alpha_i^{\text{SCS}}(i\omega) = \alpha_i^{\text{TS}}(i\omega) + \alpha_i^{\text{TS}}(i\omega) \sum_{i \neq j} \Theta_{ji} \alpha_i^{\text{SCS}}(i\omega), \quad (2.47)$$

which has to be solved self-consistently non the less [29].

A third correction, that alters the TS-SCS scheme, is the many-body dispersion (MBD) method of Tkatchenko et. al. [28, 30, 31]. The main differences of this method to the previous ones are two-fold. On the one hand, the contributions of each atomic site to the self-consistent screening equation, i.e. the interaction term of 2.46, is replaced by contributions from the sum of coupled spherical harmonic oscillators (HO) with a Gaussian smearing: $n_{\text{HO}}(\mathbf{r}_i) = (\pi^{3/2} R^3) \exp[-\mathbf{r}_i^2 / (2R^2)]$. The atomic polarizabilities are thus replaced by those of the $i = 1 \dots N$ HOs

$$\alpha_i^{\text{SCS}}(i\omega) = \alpha_i^{\text{TS}}(i\omega) + \alpha_i^{\text{TS}}(i\omega) \sum_{i \neq j} \mathcal{T}_{ji} \alpha_i^{\text{SCS}}(i\omega). \quad (2.48)$$

Here, the dipole interaction tensor, $\mathcal{T}_{ji} = \nabla_j \otimes \nabla_i W(|\mathbf{r}_j - \mathbf{r}_j|)$ mediates the interaction between two spherical Gaussian distributions with the Coulomb-like interaction $W(|\mathbf{r}_j - \mathbf{r}_j|) = \text{erf}[|\mathbf{r}_j - \mathbf{r}_j| / (\sqrt{2}R)] / |\mathbf{r}_j - \mathbf{r}_j|$. By virtue of this

concept, much computational time can be saved since the spatial contributions of 2.48 can be carried out analytically beforehand and stored in a matrix.

On the other hand – and conceptually more important – long-range many-body interactions are introduced with the random phase approximation (RPA) [32, 33]. By summing up all Feynman diagrams of the “ring” type up to infinite order, long-range correlation effects naturally emerge due to an effective screening potential. We take the frequency-dependent density-density response function $\chi(\mathbf{r}, \mathbf{r}', i\omega)$ to obey a Dyson-like integral equation

$$\chi_\lambda = \chi_0 + \chi_0 \lambda v(|\mathbf{r} - \mathbf{r}'|) \chi_\lambda. \quad (2.49)$$

The parameter λ connects the interaction via the Coulomb-type potential v , which here will be $v(|\mathbf{r} - \mathbf{r}'|) = W(|\mathbf{r}_j - \mathbf{r}_j'|)$, to the non-interacting response function χ_0 , constructed from the KS orbitals. This interaction is adiabatically connected via λ , hence the contribution to the correlation energy is taken in the framework of the adiabatic-connection and fluctuation-dissipation theorem (ACFD) [34]:

$$E_C = \frac{-1}{2\pi} \int_0^\infty d\omega \int_0^1 d\lambda \mathbf{Tr} [(\chi_\lambda(\mathbf{r}, \mathbf{r}', i\omega) - \chi_0(\mathbf{r}, \mathbf{r}', i\omega)) v(|\mathbf{r} - \mathbf{r}'|)]. \quad (2.50)$$

Consequently, the MBD method accounts for long-range correlation effects between valence electrons with intermediating quasi-particles that are modeled by spherical quantum harmonic oscillator response functions, located at the atom sites. From benchmarks and conclusions in the above cited reports, it follows that the MBD description of van der Waals-interactions should be especially suited for large molecules weakly bond to metal surfaces where the screening due to quasi-free metal electrons plays an important role.

2.5 Computational Implementation

In the preceding paragraphs, the foundations for DFT calculations have been laid. Due to the complications involved and the computing power demanded, actual DFT calculations are usually done on a multi-CPU cluster with software packages maintained by a large scientific community. Among different choices available, we use the Vienna Ab-initio Simulation Package (VASP) [35, 36, 37, 38]. In the following paragraphs a brief overview about this code and the kind of approximations and computational implementations that are used, will be given.

2.5.1 The Kohn-Sham Scheme in k-Space

In section 2.2 it was shown that the many-electron problem of any system can be mapped on an effective single-particle problem with the SE

$$\left[-\frac{1}{2} \nabla^2 + V_{\text{KS}}(\mathbf{r}) \right] \phi_i(\mathbf{r}) = \varepsilon_i \phi_i(\mathbf{r}). \quad (2.51)$$

In order to simulate a molecular layer on a metal surface, we exploit the translational symmetry of the problem by investigating a part of the whole structure that is sufficient to inhibit all constituents and use periodic boundary conditions, which then describes an infinitely large system. Note that this necessarily involves the z -direction too, which leads to stacked layers of the interface and is commonly referred to as the *repeated slab-approach*, see e.g. [39]. By virtue of translational symmetry, we can make use of Bloch's theorem [40] and express the wave-function with the wave vector \mathbf{k} and the band index i :

$$\phi_i(\mathbf{r}) \rightarrow \phi_{i\mathbf{k}}(\mathbf{r} + \mathbf{R}) = \phi_{i\mathbf{k}}(\mathbf{r})e^{i\mathbf{k}\mathbf{R}}, \quad (2.52)$$

with \mathbf{R} being a vector that leaves the Hamiltonian invariant.

Any local observable, like $n(\mathbf{r})$, is then given by an integral over \mathbf{k} , where Ω is taken to be the first Brillouin zone (BZ) and $c_{i\mathbf{k}}$ the occupation number of the state $|i\mathbf{k}\rangle$:

$$n(\mathbf{r}) = \frac{1}{\Omega} \sum_i \int_{\Omega} d^3\mathbf{k} c_{i\mathbf{k}} |\phi_{i\mathbf{k}}(\mathbf{r})|^2. \quad (2.53)$$

On the computer we will naturally replace the integration by a summation over a sample of \mathbf{k} -points in the first BZ, weighted with $w_{\mathbf{k}}$:

$$n(\mathbf{r}) = \frac{1}{\Omega} \sum_{i,\mathbf{k}} (\Delta\mathbf{k})^3 w_{\mathbf{k}} c_{i\mathbf{k}} |\phi_{i\mathbf{k}}(\mathbf{r})|^2. \quad (2.54)$$

The upper bound of the sum over \mathbf{k} introduces a convergence parameter such that the BZ can be sampled with a number of discrete points that are weighted. What has to be specified in the program is the number of sampling points per spatial direction n_j , such that the \mathbf{k} -point mesh is sampled with the spacing, e.g. in j -direction with

$$\Delta k_j = \frac{2\pi}{d n_j}, \quad (2.55)$$

d being the size of the unit cell in the specific direction. In this work, we typically work with Monkhorst-Pack grids [41] from $4 \times 4 \times 1$ to $8 \times 8 \times 3$ sampling points, leading to around hundred sampling points, which can be reduced by VASP with the help of symmetry operations. The number of bands is typically of the order of electrons in the system, making the summation relatively fast on the computer. There are some technicalities involved when sampling the BZ. One of these could be mentioned at this point: when performing integrals of entities like energy etc. over the BZ, one encounters discontinuities in these entities in metal systems at the Fermi edge, which is usually mathematically treated with step-functions. On the computer, however, these hard steps have to be replaced by an appropriate kind of smearing, which is done in our case by the method of Methfessel and Paxton [42].

For modeling the wave-functions, we can use a basis of plane waves:

$$\phi_{i\mathbf{k}}(\mathbf{r}) = \frac{1}{\sqrt{\Omega}} \sum_{\mathbf{p}} c_{\mathbf{p}i\mathbf{k}} e^{i(\mathbf{p}+\mathbf{k})\mathbf{r}}, \quad (2.56)$$

where usually the cutoff is taken to obey the condition $|\mathbf{p} + \mathbf{k}|^2 < 2E_{\max}$, with the energy cutoff E_{\max} at around a few hundred eV. It should not be confused that here we denote the reciprocal space vectors with \mathbf{p} and the wave-numbers of the plane waves with \mathbf{k} . In the basis of the Fourier coefficients, the SE is reduced to a matrix eigenvalue equation for each k-point \mathbf{p} of the form

$$\sum_{\mathbf{p}'} H_{\mathbf{p}\mathbf{p}'\mathbf{k}} c_{\mathbf{p}'\mathbf{k}} = \epsilon_{i\mathbf{k}} c_{\mathbf{p}\mathbf{k}}, \quad (2.57)$$

with the Hamilton matrix consisting of the diagonal kinetic contribution and the Fourier transform of the Kohn-Sham potential $\tilde{v}_{\text{KS}}(\mathbf{p} - \mathbf{p}')$,

$$H_{\mathbf{p}\mathbf{p}'\mathbf{k}} = \frac{1}{2}|\mathbf{k} + \mathbf{p}|^2 \delta_{\mathbf{p}\mathbf{p}'} + \frac{1}{\Omega} \tilde{v}_{\text{KS}}(\mathbf{p} - \mathbf{p}'). \quad (2.58)$$

The main computational effort involved will thus be the diagonalization of large matrices.

2.5.2 The PAW Method

Although plane waves are a very convenient basis to compute matrix elements or use the fast Fourier transformation (FFT) to rapidly change between reciprocal- and real-space, they impose problems related to core-electrons and the rapid oscillations of wave-functions close to the nuclei. In the vicinity of the nuclei the wave-functions vary strongly within small regions and have high kinetic energies, whereas in the inter-atomic regions they have low energies and are relatively smooth and responsive to the surrounding. Because of the former, a large cut-off would be necessary to expand a wave-function into plane waves, which is computationally very demanding.

There are several ways to overcome this problem, one feature that most of them have in common is to treat the atomic regions and the interatomic regions separately. Examples that could be mentioned here are the augmented plane-wave (APW) method [43, 44], that can be altered to the linearized augmented plane-wave (LAPW) method [45] or the orthogonalized plane-wave (OPW) method [46]. In the OPW method, one uses plane waves which are orthogonalized to the core states as a basis for the valence states, which effectively reduces the need for large expansion cut-offs.

Pseudo-potentials can be seen as an extension of the OPW method. Here, inside a sphere of given radius r_c , the wave-function of valence electrons is replaced by an auxiliary, smooth pseudo-wave-function, so is the potential [47, 48]. In VASP it is possible to use pseudo-potentials, in this work however, we use the pseudo-potentials of the projector augmented wave (PAW) method, which are delivered and maintained by the community [49, 50].

2.6 Photoemission Tomography

In the course of this section a short overview on the technique of photoemission tomography (PT) will be given. Angle-resolved ultra-violet photoelectron spectroscopy (ARUPS) is a standard experimental method to study the electronic structure of a material. The technique dates back to the 1970s and uses the photoelectric effect: photons from a monochromatic source with the energy ω can transfer energy when scattering with matter such that electron-emission can occur. In a simple picture, first the binding energy of the electron E_i has to be invested, then the work function, i.e. the energy needed to bring the electron from the sample into vacuum, has to be overcome. The resulting photoelectron energy is then the net of the ingredients [51]:

$$E_{\text{kin}} = \omega - E_i - \Phi. \quad (2.59)$$

This energy and the angle-dependence of these photoelectrons carry information of the electronic structure of the material.

In order to be able to describe this process from a theoretical point of view, we take the energies (and its dispersion with \mathbf{k}) and the wave-functions of the Kohn-Sham system from the DFT calculations and simulate the interaction with the photons. To this end, we use the *one-step model of photoemission* for this purpose [52, 53], which can be seen as Fermis golden-rule (first order perturbation theory in the interaction). The angle-resolved photoelectron intensity $I(\theta, \phi, E_{\text{kin}})$ is proportional to the transition matrix elements from initial states $|i\rangle$ to the final state $|f\rangle$ with the interaction of the photon field \mathbf{A} (minimal coupling) and restricted by energy conservation:

$$I(\theta, \phi, E_{\text{kin}}) \propto \sum_i |\langle f | \mathbf{p} \mathbf{A} | i \rangle|^2 \delta(\hbar\omega - E_i - \Phi - E_{\text{kin}}). \quad (2.60)$$

The problematic part this expression is how to simulate the final state. In the plane-wave final state approximation, we use plane waves, which is a coarse approximation but is reported to work very well in many cases [54, 55, 56, 57].

Chapter 3

Results

3.1 Geometry Relaxations

3.1.1 Adsorption Geometry

As a first step, we study the adsorption of coronene on the (111)-surfaces of Au, Ag and Cu and determine the equilibrium adsorption sites. Since coronene is a flat molecule with rotational symmetry, we expect the molecules to have the following degrees of freedom: the lateral position (i.e. x - and y -coordinate) on the surface, the rotational angle with respect to the metal lattice (the so-called azimuthal orientation) and the adsorption height above the metal surface (z -coordinate). While the latter is determined self-consistently in the ionic relaxation process, one has to take care of the lateral position and the rotational angle manually as an input parameter in the calculation.¹ The reason is that, there is a multitude of local energy minima on the potential energy landscape and the typical ionic relaxation schemes only guarantee to find a nearby local minimum, but not the global energy minimum.

In doing so, we calculated the adsorption energy for different sets of parameters and chose the most favorable ones for further examinations. In terms of unit cells, low-energy electron diffraction (LEED) experiments for coronene on Au(111) [58] and coronene on Ag(111) [59] both found a supercell with an epitaxial matrix of

$$\begin{bmatrix} 4 & 0 \\ 0 & 4 \end{bmatrix}. \quad (3.1)$$

For the case of coronene on Cu(111), experimental data [60] suggests an epitaxy matrix of

$$\begin{bmatrix} 5 & 1 \\ -1 & 4 \end{bmatrix}, \quad (3.2)$$

¹Other than that, there exist several more automatic techniques to find minima in the adsorption energy-landscape, such as thermal annealing, genetic algorithms or database-powered machine learning codes that would, in this case, be too sophisticated tools for the purpose.

where the unit-cell vectors were taken to be $\mathbf{b}_1 = a/\sqrt{2}(1,0)^T$ (i.e. the $[\bar{1}10]$ -direction of the (111) fcc surface) and $\mathbf{b}_2 = a/(2\sqrt{2})(1,\sqrt{3})^T$. In the expressions for the unit vectors a is the lattice constant, for which the values $a_{\text{Au}} = 4.078 \text{ \AA}$, $a_{\text{Ag}} = 4.085 \text{ \AA}$ and $a_{\text{Cu}} = 3.615 \text{ \AA}$ were used.

As a starting point, total energies for the three high-symmetry adsorption sites depicted in figure 3.1 were computed for 2 different rotational angles (0° and 30°). The rotational angle ϕ is defined as the positive rotation between the zig-zag-direction of the molecule (as defined in graphene) and the $[\bar{1}10]$ -direction of the respective fcc-surfaces, see also figure 3.2. In this case, the total energies allow for a direct comparison since they have been computed in the same fashion and the sizes of the unit cells are the same. The results are shown in table 3.1.

Although the differences in total energies are close to the typical error of such

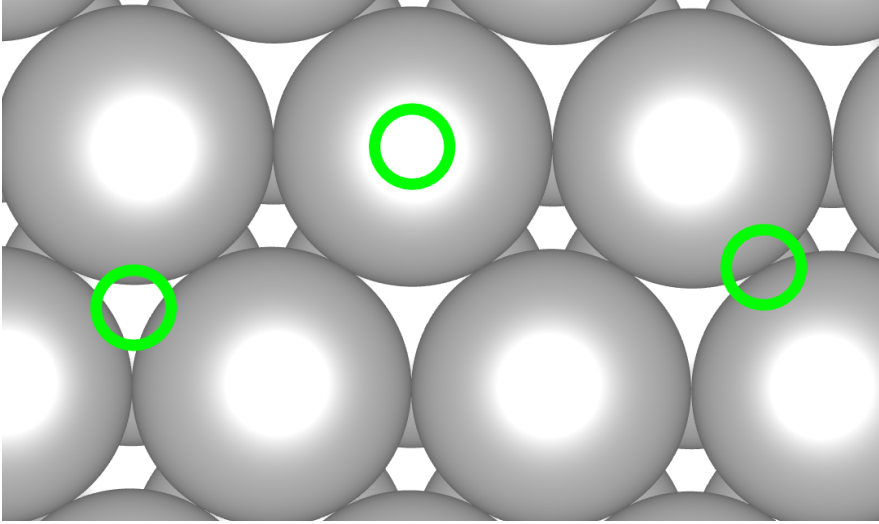


Figure 3.1: Adsorption sites for the center of the coronene molecules on the (111)-surface, denoted from left to right: center, top, bridge.

Table 3.1: Total energies of different adsorption sites of coronene on Au(111), Ag(111) and Cu(111) computed with the PBE exchange-correlation functional and TS method for van der Waals-corrections with optimized parameters (most favorable ones highlighted).

	Au, 30°	Au, 0°	Ag, 30°	Ag, 0°	Cu, 25°	Cu, 0°
Center	-551.034	-551.040	-537.276	-537.349	-710.752	-710.875
Top	-550.950	-551.012	-537.098	-537.036	-710.814	-710.604
Bridge	-551.007	-551.007	-537.271	-537.341	-710.754	-710.843

calculations (around 2 meV/atom), the energetically most favorable configu-

rations (highlighted in the table) were the same on each surface, which gave confidence to choose the center site for further calculations.

In a second step, we varied the rotational angle of the molecule (center position), the results are shown in figure 3.3. These computations were done

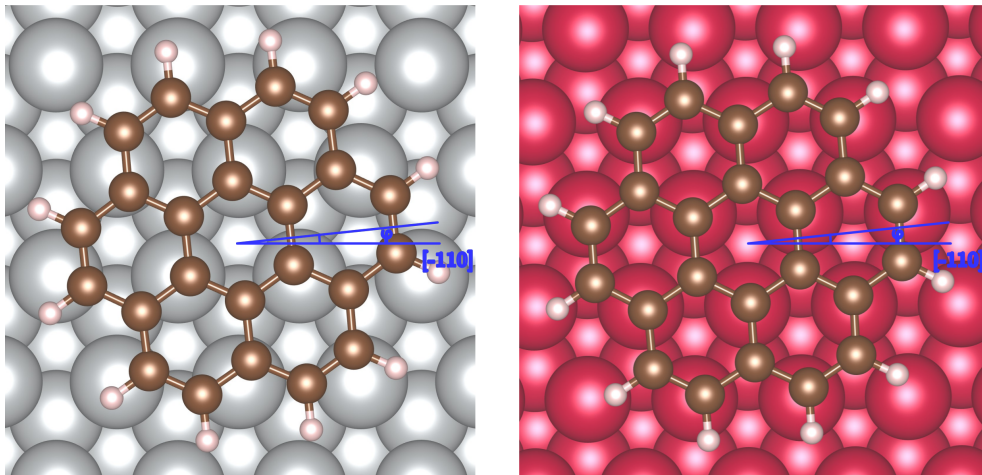


Figure 3.2: Optimized adsorption sites of coronene on Ag(111) (left) and coronene on Cu(111) (right). The rotational angle ϕ is defined as the positive rotation between the zig-zag-orientation of the molecule and the fcc $[\bar{1}10]$ -direction.

in two individual steps: one in which the positions of all atoms were held fixed, and another where the atoms in the molecule as well as the two topmost layers of the respective metal surface were allowed to relax. This resulted in energetically converged positions at the price of small deviations from the pre-set angles (maximum 1°). Around the respective energy minimum, the step-size for the rotational angle was refined to this value, such that the angular differences were in the order of movements the molecule would make in the process of geometric relaxation during the DFT calculation.

One observes that the minima lie around 5° , where coronene on silver shows the smoothest curve, coronene on gold the most prominent and coronene on copper a less distinct minimum. The minima between 4.5° and 6.5° can be explained with intermolecular interaction upon adsorption: with this orientation, the interdigitated H-atoms minimize the energy, as can be seen when bringing the two panels of figure 3.2 together. The minimum found for the case of coronene on silver is also supported by experimental data from a STM study [4]. It is also apparent that the curve for coronene on copper does not resemble the other two in the region around 15° , where, contrastingly, a second minimum appears. This fact is due to the smaller size of copper atoms and the resulting lattice structure, allowing for another energetically favorable

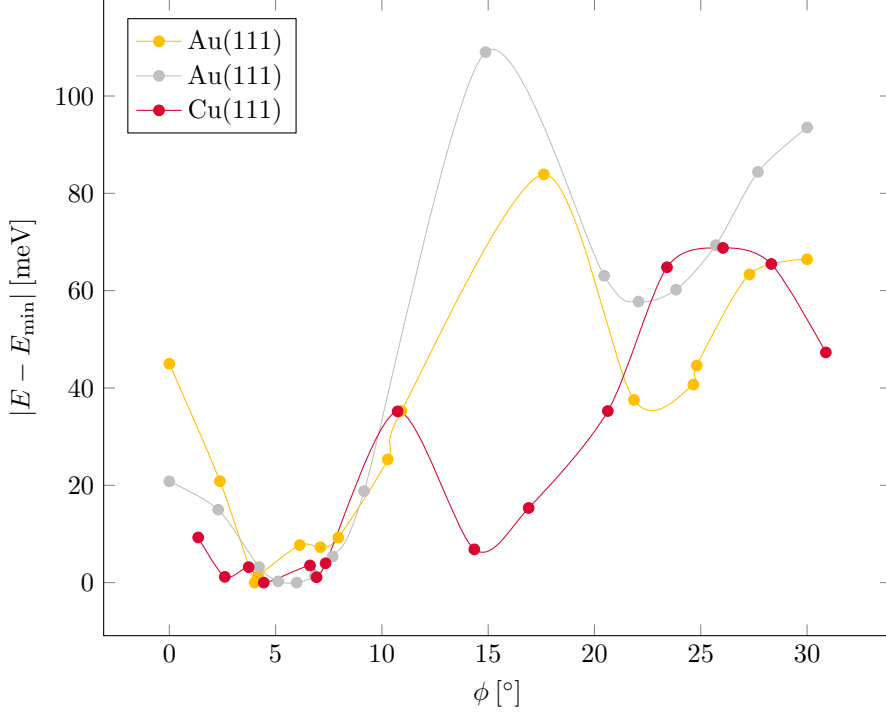


Figure 3.3: Total energies of coronene on the (111)-surfaces of gold, silver and copper with respect to the rotational angle of the molecule. The angle of 0° is defined such that the zig-zag orientation of coronene is in the $[\bar{1}10]$ -direction of the substrate. Rotations further than 30° are redundant because of the molecule’s symmetry. The calculations were done with the PBE exchange-correlation functional and the TS van der Waals-correction with optimized parameters.

position of the coronene molecule.

Table 3.2 exhibits the adsorption energies, the adsorption heights as well as the deviations of the z -coordinates of surface and molecule respectively. Here, and in the following, we define the adsorption energy as the energy of the interface minus the sum of 1 ML of coronene molecules and the substrate, i.e.

$$E_{\text{ads}} = E_{\text{int}} - (E_{\text{mol}} + E_{\text{sub}}). \quad (3.3)$$

Note that for calculating both the energies of the substrate and the molecules, atomic positions were held fixed. The energies and distances draw a clear picture: coronene on gold and silver behave similar in terms of adsorption energy and distance, whereas coronene on copper is more strongly bound and located at a shorter distance. For the adsorption height the following convention is used throughout this thesis. We take the average z -value of all carbon atoms

of the coronene molecule and subtract from that the average z -value of the topmost metal layer. While coronene molecules in the gas phase have a perfectly flat geometry, upon adsorption we see a mild distortion in such a way that inner carbon atoms are further away than the outer ones. Vice versa, the surface atoms slightly rearrange due to molecule-substrate interaction. Both phenomena are not exceptionally strong in this case, but their effects can be seen in the two last rows of the table: the most reactive substrate, copper, deforms the molecule the most, the least reactive substrate, gold, is rearranged the most upon adsorption. Note that the given errors are statistical errors from accounting for counting different z -coordinates for different atoms that would have to be smeared out with the errors of the DFT calculation. Consequently, the figures of table 3.2 should be seen as a trend rather than absolute values.

Table 3.2: Adsorption energies and adsorption heights of coronene on Au(111), Ag(111) and Cu(111) at optimized sites.

	Au	Ag	Cu
E_{ads} [eV]	-2.178	-2.151	-2.465
d [Å]	3.19 ± 0.08	3.10 ± 0.04	2.87 ± 0.06
Δz_{sur} [Å]	0.04	0.02	0.02
Δz_{mol} [Å]	0.04	0.03	0.05

Having determined the adsorption geometry for each system, more precise computations could be utilized. In particular, we refined the \mathbf{k} -mesh from $4 \times 4 \times 1$ to $8 \times 8 \times 1$ and allowed for a energy-cutoff of 500 eV. As described in the preceding chapter, the energy and the electronic structure of the systems under consideration depend also on the chosen exchange-correlation functional and its van der Waals-correction, which will be addressed to the next paragraph.

3.1.2 Van der Waals Schemes

In many systems the general adsorption geometry and the electronic structure of the systems under consideration are fairly independent of the chosen DFT functional and the according Van der Waals-correction. In systems that are dominated by physisorption, however, the adsorption energy and the adsorption height are strongly influenced by the computational treatment of the non-local-interactions within the system. In order to investigate, how sensitive the adsorption structure is with respect to the treatment of van der Waals-interactions, we want to compare results from calculations that have been carried out with different methods. It follows from the results shown above that the adsorption of coronene on Au(111) is most sensitive to these subtle forces, since the binding is the weakest of all three systems. Accordingly, the case of coronene on gold was examined further, utilizing the three different van der

Waals-correction-schemes that have been described in section 2.4.

The results can be seen in table 3.3, where the adsorption energy, the average adsorption height as well as the surface and molecule rearrangements are shown for the four cases: The TS method with the optimized parameter from Ruiz et. al. [27], the TS method with SCS, the MBD method with default van der Waals-parameter and the MBD method with van der Waals-parameter obtained with the SCS method. A fifth method, the MBD method with the optimized van der Waals parameter from Ruiz et. al. [27], was also tested, we do not show the results in table 3.3 however, since the results are almost identical to the MBD-SCS data.

Table 3.3: Adsorption energies and adsorption heights of coronene on Au(111) for the PBE functional with different van der Waals-correction schemes: Tkatchenko-Scheffler (TS), TS with self-consistent screening (TS-SCS), many-body dispersion (MBD) and MBD with SCS.

	TS	TS-SCS	MBD	MBD-SCS
E_{ads} [eV]	-2.178	-3.986	-1.674	-1.410
d [Å]	3.19 ± 0.08	3.22 ± 0.10	3.32 ± 0.07	3.33 ± 0.06
Δz_{sur} [Å]	0.04	0.07	0.04	0.03
Δz_{mol} [Å]	0.04	0.02	0.03	0.03

The results for the adsorption height draw a clear line: the more sophisticated the van der Waals-correction, the greater the adsorption height with the largest step towards the MBD methods. To the best of our knowledge, there is, unfortunately, no experimental data for this system to which our results could be compared to. It should therefore serve as a reference to compare these values to the closest members of the aromatic family, namely benzene (C_6H_6) and hexa-peri-hexabenzocoronene (HBC, $\text{C}_{42}\text{H}_{18}$). The experimental data [61] and corresponding DFT simulations [62] for benzene on Au(111) report an adsorption height of $d = 3.7 \text{ \AA}$ and a binding energy of $E_{\text{B}} = -0.64 \text{ eV}$. For HBC on Au(111) the only available figure is an adsorption height of $d = 3.09 \text{ \AA}$, although measured at a coverage of 0.3 ML [63]. When comparing the adsorption heights, we find that our results lie in between the smaller and the bigger molecule, indicating that the longer adsorption height of the MBD method should be preferred in order to match the pattern. In terms of binding energies, we can only take the value of benzene with a binding energy per carbon atom of $E_{\text{B}}/\text{C} - \text{atom} = -0.11 \text{ eV}$. Interpolated to the number of carbon atoms of coronene, this would lead to a binding energy of $E_{\text{B}} = -2.56 \text{ eV}$. Note that this value cannot be trusted due to the different adsorption heights such that these argumentations are everything else than compelling and should only be seen as side remark as the physisorption of different sizes of aromatic molecules are subjected to the subtle interplay between molecule and sur-

face structure, intermediated by van der Waals-forces. The results of van der Waals-correction schemes are concluded by further remarking that the case of coronene is indeed very sensitive to the computational treatment of dispersion forces (as can be seen in strong deviations of the respective binding energies). For further calculations we stick to the TS scheme since this is computationally much less demanding and typically the electronic structure will be less affected by the choice of method than the adsorption energies.

3.2 Electronic Structure

When talking about the electronic structure of a quantum mechanical system, an important measure is usually the electronic density of states (DOS), which is here averaged over spatial regions and evaluated in a certain range of energy. As a starting point, the total DOS of the three systems is depicted in figure 3.4. The curves have been normalized such that the maximum equals 1 and are

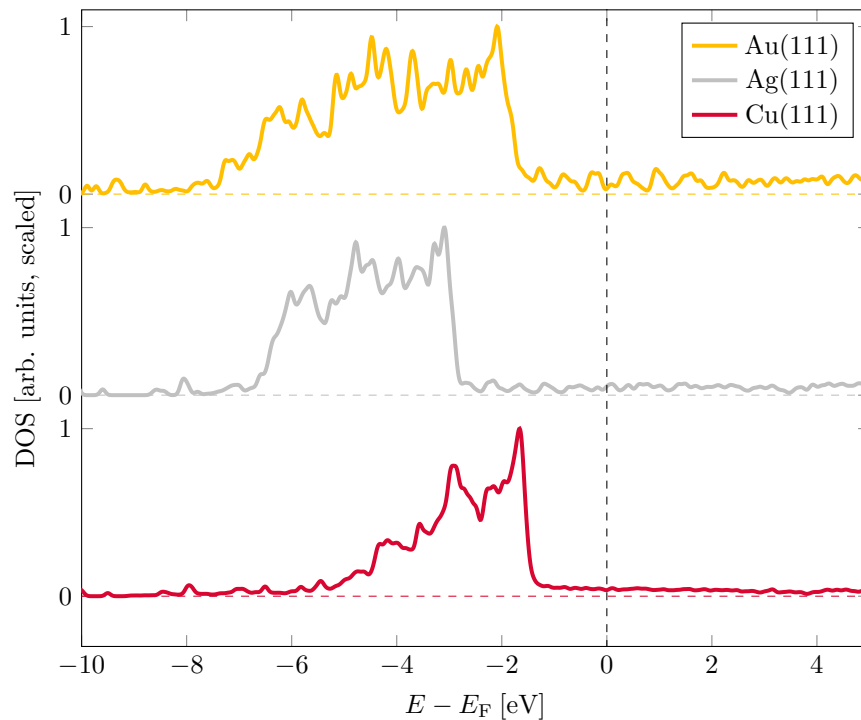


Figure 3.4: DOS of the composite systems of coronene on the adsorbates Au(111), Ag(111) and Cu(111) respectively.

merely used for qualitative comparison of the systems. Energetically below the Fermi edge, the most prominent peaks stem from the metal d-bands. In order to distinguish substrate from molecular features or features that arise from the hybridization between molecule- and substrate-states, it is useful to project the

DOS (pDOS) on atomic orbitals, which is shown for the case of gold and silver in figure 3.5. Note that the values of the interface and the substrate have been

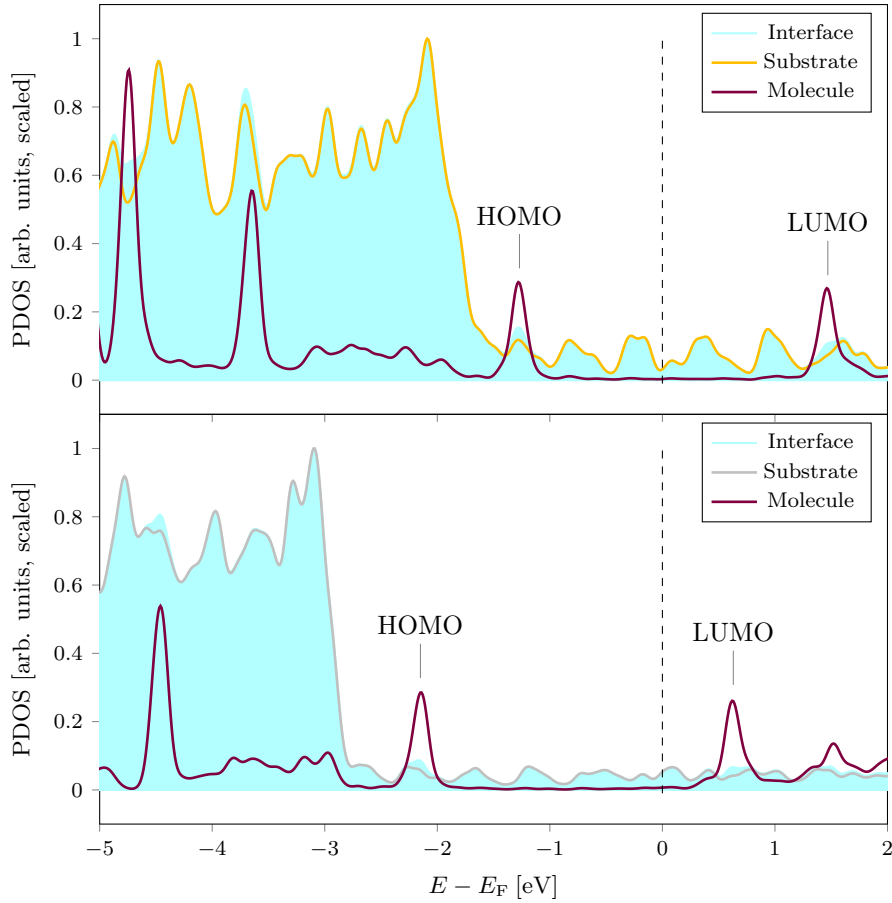


Figure 3.5: The pDOS of the interface coronene-Au(111) in the upper panel and of coronene-Ag(111) in the lower panel.

scaled to the same value, whereas the curve for the molecule has been scaled with a factor of 67.3 (top) and 136.6 (bottom) to allow for a direct comparison. When comparing all three curves for one system, it is apparent that most of the DOS is resulting from the substrate and the molecule contributes very little and only at distinct positions in energy.

For the case of coronene/Au(111) and coronene/Ag(111) (figure 3.5), it is possible to assign the peaks closest to the Fermi level to the HOMO and LUMO, respectively. In the case of coronene/Cu(111) however, it is not possible to be certain about the HOMO position, since the first peak below the Fermi edge is energetically already in the range of the Cu d-bands, which can be seen in the upper panel of figure 3.6. This behavior must be seen as a shortcoming of the PBE-functional, which results in the Cu d-bands being

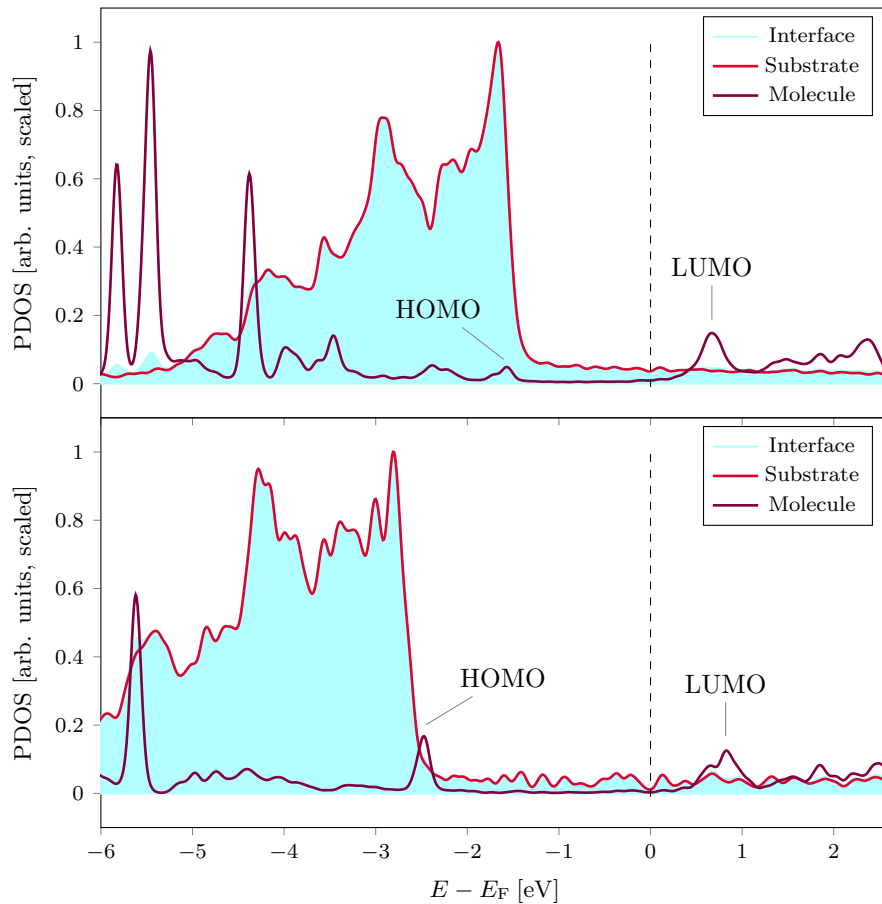


Figure 3.6: The pDOS of the interface coronene-Cu(111). Upper panel: evaluated with the GGA functional. Lower panel: evaluated with the HSE functional.

at a too low binding energy, see e.g. [64]. In order to overcome this behavior, another calculation with a hybrid functional, the Heyd-Scuseria-Ernzerhof (HSE) functional, was done. The resulting pDOS can be seen in the lower panel of figure 3.6. Here, the HOMO is more prominent and lies energetically above the Cu d-bands, although by a rather small margin.

In order to characterize the electronic structure of a composite system, it is fruitful to look at how charges rearrange upon adsorption. In general, a metal surface exhibits a surface dipole due to the non-vanishing electron density outside the surface [65]. This dipole layer can be reduced due to the electron density of the molecule, which repels charges as a result of the Pauli principle (*push-back-effect* [66, 67]). Figure 3.7 gives an overview of this behavior for the three different systems. Horizontally, the three columns represent the three different adsorbates gold, silver and copper, while vertically the change in

electrostatic potential ΔE_{pot} , the transferred charge Q and the charge-density difference $\Delta\rho$ are plotted versus the z -axis, respectively. The dotted lines in the background represent the charge density, where the magnitudes have been scaled to mark the z -positions of the molecule and the respective surface atoms as references.

Starting from the lowest row, $\Delta\rho(z)$ shows the plane-averaged charge-density difference, which is defined as

$$\Delta\rho(z) = \rho_{\text{tot}}(z) - [\rho_{\text{mol}}(z) + \rho_{\text{sub}}(z)]. \quad (3.4)$$

Thus, in addition to the charge density of the full system ($\rho_{\text{tot}}(z)$), we have performed two additional calculations, one in which only the molecule monolayer is present and one for the substrate. Note that in these two calculations, the atomic positions have been fixed to those of the full system and that the charge densities have been integrated over the x, y -plane. We now clearly see a rearrangement of positive charge in the outer region of the surface as the result of a diminishing surface dipole (push-back-effect). Conversely, this results in a reduced electron density at the position of the molecule, with the preferred region of origin being the one closer to the surface and with the exception of the molecule center. Coronene is a typical member of the aromatic family with delocalized π -orbitals in which the electrons can move considerably free and thus push back the electrons of the surface dipole, rather than the localized electrons of the σ -system, where we even see a slight positive net charge rearrangement upon adsorption.

Integrating the difference in charge density over the z -direction from z_0 to the point z gives the net change in charge at that point, which can be seen in the middle panel and is defined as

$$Q(z) = \int_{z_0}^z dz' \Delta\rho(z'), \quad (3.5)$$

where we take z_0 to be out in the vacuum region [68]. When starting outside from the vacuum, we see a “lack of negative charge” that peaks in the middle between the molecule and the surface.

Turning to the uppermost panels, integrating once more over z gives the plane-averaged change in the electrostatic potential induced by the interaction of the molecule with the substrate (here: $\Delta E_{\text{pot}}(z)$). Away from the gap in the vacuum direction, this potential relative to the Fermi energy can be related to the change in work function $\Delta\Phi$ of the system, i.e. the change in energy necessary to remove one electron from the system into the vacuum. The values of Φ itself were determined as 4.55 eV, 3.57 eV and 3.76 eV for coronene on gold, silver and copper respectively. The work function of the uncovered (111)-surfaces are 5.25 eV for gold, 4.40 eV for silver [69] and 4.78 eV for copper [70], such that we get a work function change of 0.70 eV (Au), 0.83 eV (Ag) and 1.11 eV (Cu) which is also indicated in black color in the

upper panel of figure 3.7. We thus see a stronger work function change when going from the from less reactive surfaces to the more reactive. This behavior agrees with statements made before and again reflects the way how adsorption on copper leads to a stronger molecule-surface-interaction than in the other cases. It should also be noted that the push-back-effect is stronger in the case of Cu due to the shorter adsorption height of the coronene molecules.

3.3 Photoemission Angular Distributions

The most direct experimental method to explore the electronic structure of surfaces is photoemission spectroscopy. Using UV-light, ultra-violet photoemission spectroscopy (UPS) gives access to the DOS. When taking into account also the angular dependence of the photoemitted electrons, even further insights can be gained.

In order to study the effects of the adsorption on the electronic structure of the coronene molecule, we first simulated 1 ML of coronene without substrate. In contrast to a single molecule, the 1 ML structure shows inter-molecular interaction, which allows us to separate the effects of molecule-molecule- and molecule-substrate-interaction. For the case of 1 ML of coronene, the defining equation 2.60 for the photoemission intensity is reduced from a summation over all bands and \mathbf{k} -points to only one single molecular orbital as the initial state. Since the summation over \mathbf{k} -points leads to delta-functions that project out the respective point in the Brillouin zone, these peaks have to be smeared-out by Gaussian-type distributions on the computer, where we used a broadening of $\Delta\mathbf{k} = 0.05 \text{ \AA}^{-1}$. Moreover, the energy resolution of the photoemission energy in the experiment is not sharp, such that we also use a broadening in energy that was set to $\Delta E = 0.05 \text{ eV}$.

We now look at the HOMO of the molecule, which is a 2-fold degenerate state. The left and middle panel of figure 3.8 show the respective photoemission angular distribution maps of each state, whereas the right panel is the superposition of both. In general, we see a clear six-fold symmetry of the HOMO features, which represents the geometry of the molecule. It is also noticeable that the molecules are rotated with respect to the main symmetry axes (here the value of the optimized rotational angle for the case of gold had been taken).

Only recently, a method has been developed which can be used for adsorbates on substrates. When approximating the final state with a plane wave, the influence of the bulk states is overestimated since each electron can contribute equally to the photoemission current, regardless of its origin inside the bulk. In practice, however, electrons that are nearer to the surface will be emitted more likely due to the damping of the light intensity inside the material and the fact that low-lying electrons (if they have been excited by

the incoming light-beam) will scatter from the material and will thus be effectively suppressed in the current. The way to implement a mean-free path of the scattered electrons is an exponential damping of the plane wave final state inside the bulk. This method is reported to produce excellent results for hydrocarbons on metal surfaces, e.g. for perylenetetracarboxylic dianhydride (PTCDA) on Cu(100) [71].

The photoemission angular distribution map of 1 ML of coronene can now be compared to those of the HOMO of the coronene-interfaces with Au(111) and Ag(111), which can be seen in figure 3.9, where the energy corresponds to the HOMO peaks from figure 3.5. Note that the 1 ML map and the interface maps have now been symmetrized in order to represent the fact that in an actual experiment, the surface of emitting electrons is large compared to the size of the domain islands. Consequently, the data is a mix from different domain orientations, which we can simulate by applying mirror symmetry with respect to the high-symmetry axes of the structure. For the interface of coronene with Ag(111), similar features than those of the HOMO of the free-standing coronene layer can be observed, although a slight influence from the substrate is present in the background, which however still shows six-fold symmetry. For the case of coronene on Au(111), this background-structure is richer and does not show clear six-fold symmetry. The fact that the molecule-substrate-interaction is stronger for the case of Au(111) also agrees with the fact that the molecular HOMO feature lies closer to the metal d -bands than for the case of Ag(111) (see also figure 3.5). For both cases, we furthermore see deformations of the main lobes due to the interaction of the substrate.

In the course of this work, a paper with experimental and theoretical results was published [4]. Figure 3.10 was taken from this publication and shows a comparison of experimental to theoretical results for coronene on Ag(111). From the zoom-in in the lower panel, it can be concluded that the simulations fit the experimental data very well, especially in the case of the HOMO.

As discussed before, the above mentioned behavior of the substrate influence in the case of silver is even more prominent for the case of coronene on Cu(111), since the d -bands are covering the HOMO for the PBE calculation, which lead to an extra calculation utilizing the HSE functional. In figure 3.11, the two prominent HOMO and HOMO-1 (left and middle) features from the PBE calculation are compared to the HOMO feature of the HSE calculation (right map). In this case, even more influence of the substrate can be seen for the two PBE maps, whereas the HSE map shows very little influence of the substrate and looks similar to the 1 ML HOMO feature in figure 3.8. It must be noted that the broadening in energy and momentum necessary to generate these maps from discrete sets of points was set to $\Delta k = 0.05 \text{ \AA}^{-1}$ and $\Delta E = 0.05 \text{ eV}$ throughout, whereas for the HSE calculation we had to restrict to 0.1 eV for both values. This is owed to the fact that for PBE we were able to use a \mathbf{k} -mesh of $8 \times 8 \times 3$ whereas for HSE we had to restrict

to $4 \times 4 \times 1$ for computational reasons. The coarser grid in \mathbf{k} -space would produce artifacts in the photoelectron angular distribution maps if computed with the finer \mathbf{k} -space broadening. This also explains the smoothness and good contrast of the HSE map and its good agreement to the HOMO feature of 1 ML.

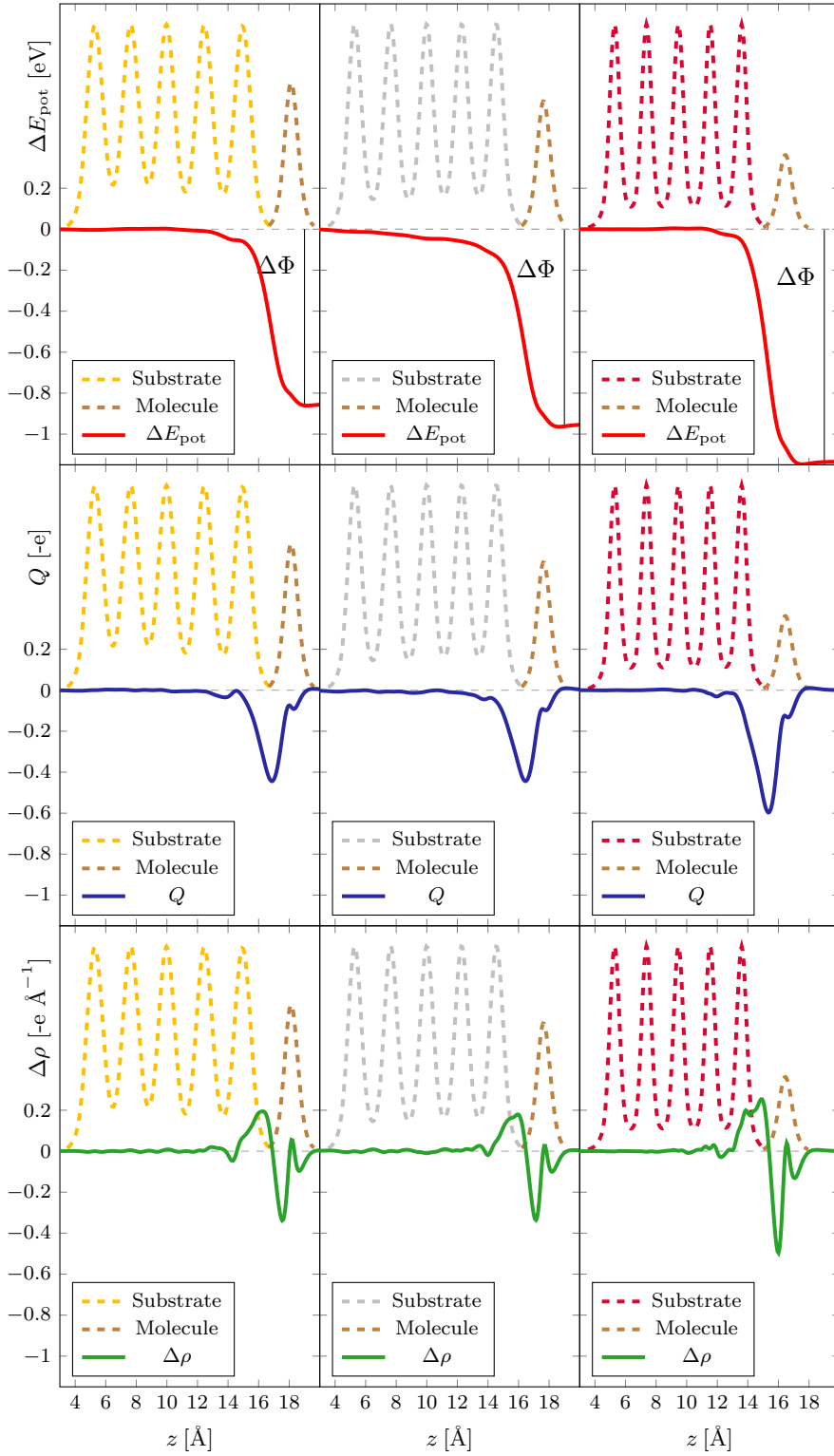


Figure 3.7: From left to right: coronene on Au(111), Ag(111) and Au(111). From top to bottom: $\Delta E_{\text{pot}}(z)$ with $\Delta\Phi$ indicating the change in work function, $Q(z)$ and $\Delta\rho(z)$. The charge-densities of the substrate (in the respective color) and those of the molecule (brown) have been added in dashed lines to indicate atomic positions (arb. units, scaled in magnitude).

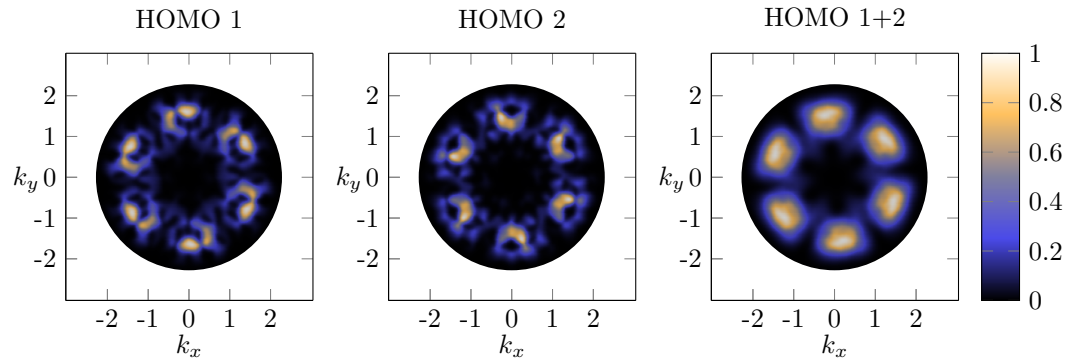


Figure 3.8: Photoemission angular distribution maps of 1 ML of free-standing coronene. Left and middle show the two degenerate states that form the HOMO (right). The k -space is measured in units of \AA^{-1} , the photoemission intensity has been normalized to 1.

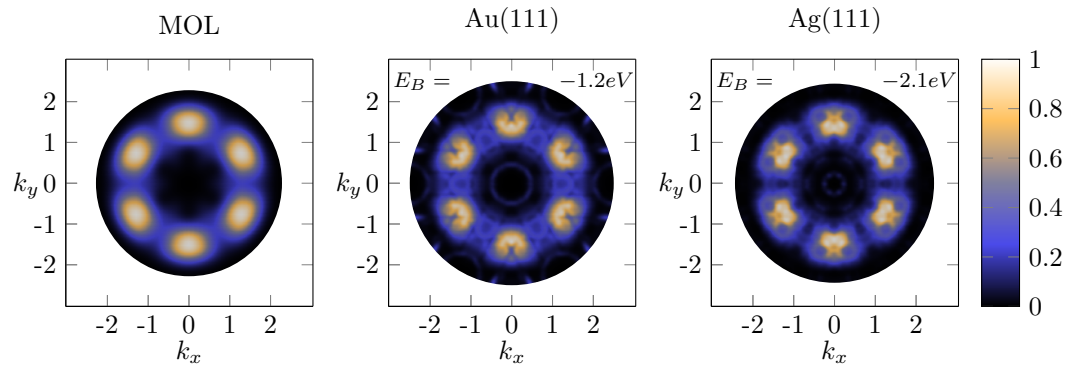


Figure 3.9: Photoemission angular distribution maps of the HOMO emission. Left is the map of 1 ML of coronene (symmetrized for comparison), in the middle coronene on Au(111) and to the right coronene on Ag(111). The k -space is measured in units of \AA^{-1} , the photoemission intensity has been normalized to 1.

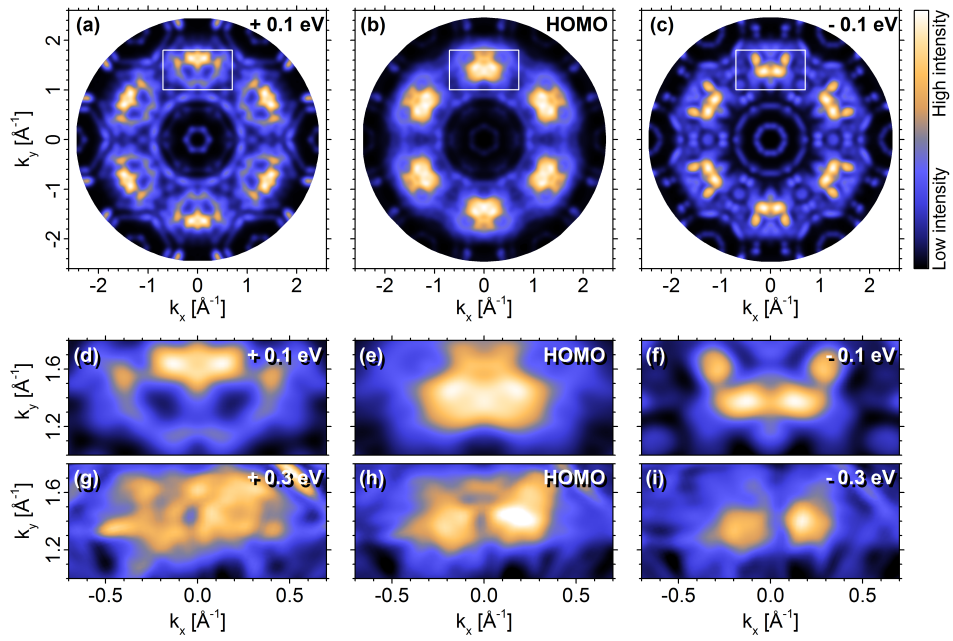


Figure 3.10: Upper panel: theoretical results for coronene on Ag(111) with the HOMO feature in the middle and binding energies of ± 0.1 eV with respect to the HOMO to the left and right. Lower panel: zoom-in of the theoretical calculations (top) compared to experimental results (bottom) respective to the above energies.

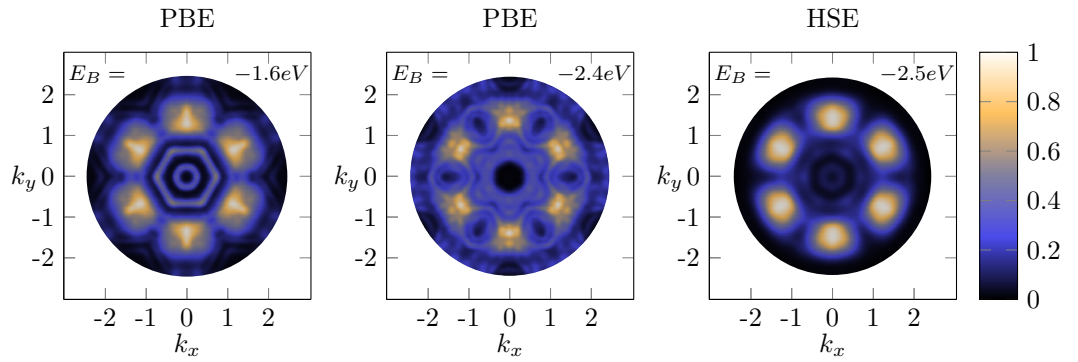


Figure 3.11: Photoemission angular distribution maps of coronene on Cu(111). Left and middle panels show the maps calculated with the PBE functional at the binding energies of -1.6 eV and -2.4 eV respectively. To the right the HOMO feature calculated with the HSE functional is shown. Note that in the latter – due to computational limitations that do not allow for a finer k -space mesh with the HSE functional – a broadening in k -space of $\Delta k = 0.1 \text{ \AA}^{-1}$ was used instead of $\Delta k = 0.05 \text{ \AA}^{-1}$. The k -space is measured in units of \AA^{-1} , the photoemission intensity has been normalized to 1.

Chapter 4

Conclusions and Outlook

In this thesis a comprehensive theoretical study of the organic-metal interfaces of coronene on the (111)-surfaces of gold, silver and copper has been conducted. In determining the optimal adsorption sites with respect to the metal surfaces, we have found an overall similarity for all three systems, where the center of the molecule has been found to be in the center position of three metal atoms. For the azimuthal orientation of coronene on the three metal surfaces, we have determined the minima to lie between 4.5° and 6.5° , which is also supported by experimental data from STM imaging. The last degree of freedom – the adsorption height – has been computed with geometry relaxations, with an emphasis on the system coronene on Au(111) since this system has been found to show the weakest binding to the surface. Having utilized three different methods for the implementation of long-range dispersion forces, we find that the adsorption height and the adsorption energy varies strongly with the methods. Experimental data for our system was not available, thus we have compared the results to the similar systems benzene/Au(111) and hexaperi-hexabenzocoronene/Au(111), where we see that the data for coronene resembles the trend in adsorption height when moving up in the family of cyclic hydrocarbons. Although problematic to compare, we have concluded to prefer the more sophisticated method of many-body dispersion. After the geometric optimization, we have studied the electronic structure of the three interfaces.

Also, regarding the density of states and the energy position of the HOMO, we have found similarities for the surfaces silver and gold. For copper however, a further calculation with a hybrid functional had to be performed in order to clarify the HOMO position. When analyzing the charge rearrangements upon adsorption, we have seen that the surface dipole gets diminished (push-back effect) in all three cases accompanied by a reduction of the work function, with the magnitude following the line of surface reactivity from gold to copper. We have not seen any significant charge transfer between surface and molecule

in any case whatsoever.

In order to simulate photoemission spectroscopy, photoemission angular distribution maps have been computed. By this virtue, comparison of the electronic states of 1 ML of coronene and the adsorbates had been possible. From this we have seen the influence of the different substrates to the HOMO states and the inter-molecular dispersion. For the case of coronene on silver, these simulations have been compared to experimental data and show good agreement.

As an outlook to further studies, we could state that the validation of our results would benefit from experimental data of the respective systems, of which only STM and ARUPS data for coronene/Ag(111) is available to this day. Especially a study of adsorption heights and energies would be desirable to clarify the question of van der Waals-corrections. Alternatively, DFT simulations of benzene with different correction schemes could be compared to the existing experiments.

Acknowledgements

First and foremost, I want to thank my supervisor Professor Peter Puschnig for his patience and his support. Fruitful discussions with the Ab-initio group at the University of Graz are furthermore acknowledged with special thanks to Daniel Lüftner for numerous discussions and his ongoing help.

I also want to thank my family and friends for their support with special thanks to Brónagh.

Simulations presented in this thesis have been calculated at the computing facilities at the Karl-Franzens-Universität Graz and at the Vienna Scientific Cluster (VSC).

Bibliography

- [1] Jaehyung Hwang, Alan Wan, and Antoine Kahn. Energetics of metal-organic interfaces: New experiments and assessment of the field. *Materials Science and Engineering: R: Reports*, 64(1):1 – 31, 2009.
- [2] Wikipedia article: Coronene. URL: <https://en.wikipedia.org/wiki/Coronene>, 10.07.2018.
- [3] Kubozono, Yoshihiro and Mitamura, Hiroki and Lee, Xuesong and He, Xuexia and Yamanari, Yusuke and Takahashi, Yosuke and Suzuki, Yuta and Kaji, Yumiko and Eguchi, Ritsuko and Akaike, Koki and Kambe, Takashi and Okamoto, Hideki and Fujiwara, Akihiko and Kato, Takashi and Kosugi, Taichi and Aoki, Hideo. Metal-intercalated aromatic hydrocarbons: a new class of carbon-based superconductors. *Phys. Chem. Chem. Phys.*, 13:16476–16493, 2011.
- [4] Christian Udhardt, Felix Otto, Christian Kern, Daniel Lüftner, Tobias Huempfer, Tino Kirchhübel, Falko Sojka, Matthias Meissner, Bernd Schröter, Roman Forker, Peter Puschnig, and Torsten Fritz. Influence of Film and Substrate Structure on Photoelectron Momentum Maps of Coronene Thin Films on Ag(111). *The Journal of Physical Chemistry C*, 121(22):12285–12293, 2017.
- [5] M. Born and R. Oppenheimer. Zur Quantentheorie der Molekeln. *Annalen der Physik*, 389(20):457–484.
- [6] Franz Schwabl. *Quantenmechanik für Fortgeschrittene*. Springer, 2005.
- [7] A. Altland and B. Simons. *Condensed Matter Field Theory*. Cambridge University Press, 2006.
- [8] Claude et. al Cohen-Tannoudji. *Quantenmechanik I + II*. Walter de Gruyter GmbH und Co. KG, Berlin, 1999.
- [9] P. Hohenberg and W. Kohn. Inhomogeneous Electron Gas. *Phys. Rev.*, 136:B864–B871, Nov 1964.

- [10] Gabriele Giuliani and Giovanni Vignale. *Quantum Theory of the Electron Liquid*. Cambridge University Press, 2005.
- [11] Wolfram Koch and Max Holthausen. *A Chemists Guide to Density Functional Theory*. Wiley-VCH Verlag GmbH, 2001.
- [12] Julien Toulouse. Introduction to density-functional theory, URL: http://www.lct.jussieu.fr/pagesperso/toulouse/enseignement/introduction_dft.pdf, 10.06.2018.
- [13] Reinier M. Dreizler and Eberhard K. U. Gross. *Density Functional Theory - An Approach to the Quantum Many-Body Problem*. Springer Verlag Berlin heidelberg New York, 1990.
- [14] W. Kohn and L. J. Sham. Self-Consistent Equations Including Exchange and Correlation Effects. *Phys. Rev.*, 140:A1133–A1138, Nov 1965.
- [15] Klaus Capelle. A bird’s-eye view of density-functional theory. *Brazilian Journal of Physics*, 36:1318 – 1343, 12 2006.
- [16] Randolph Q. Hood, M. Y. Chou, A. J. Williamson, G. Rajagopal, and R. J. Needs. Exchange and correlation in silicon. *Phys. Rev. B*, 57:8972–8982, Apr 1998.
- [17] John P Perdew, Kieron Burke, and Matthias Ernzerhof. Generalized gradient approximation made simple. *Physical review letters*, 77(18):3865, 1996.
- [18] Jianmin Tao, John P. Perdew, Viktor N. Staroverov, and Gustavo E. Scuseria. Climbing the Density Functional Ladder: Nonempirical Meta-Generalized Gradient Approximation Designed for Molecules and Solids. *Phys. Rev. Lett.*, 91:146401, Sep 2003.
- [19] Axel D. Becke. A new mixing of Hartree-Fock and local density-functional theories. *The Journal of Chemical Physics*, 98(2):1372–1377, 1993.
- [20] Iann C. Gerber and János G. Ángyán. Hybrid functional with separated range. *Chemical Physics Letters*, 415(1):100 – 105, 2005.
- [21] Jochen Heyd, Gustavo E. Scuseria, and Matthias Ernzerhof. Hybrid functionals based on a screened Coulomb potential. *The Journal of Chemical Physics*, 118(18):8207–8215, 2003.
- [22] Jochen Heyd and Gustavo E. Scuseria. Efficient hybrid density functional calculations in solids: Assessment of the Heyd-Scuseria-Ernzerhof screened Coulomb hybrid functional. *The Journal of Chemical Physics*, 121(3):1187–1192, 2004.

- [23] Jochen Heyd, Gustavo E. Scuseria, and Matthias Ernzerhof. Erratum: "Hybrid functionals based on a screened Coulomb potential" [J. Chem. Phys. 118, 8207 (2003)]. *The Journal of Chemical Physics*, 124(21):219906, 2006.
- [24] Jan Hermann, Robert A. DiStasio, and Alexandre Tkatchenko. First-Principles Models for van der Waals Interactions in Molecules and Materials: Concepts, Theory, and Applications. *Chemical Reviews*, 117(6):4714–4758, 2017.
- [25] Kyuho Lee, Éamonn D. Murray, Lingzhu Kong, Bengt I. Lundqvist, and David C. Langreth. Higher-accuracy van der Waals density functional. *Phys. Rev. B*, 82:081101, Aug 2010.
- [26] Alexandre Tkatchenko and Matthias Scheffler. Accurate Molecular van der Waals Interactions from Ground-State Electron Density and Free-Atom Reference Data. *Phys. Rev. Lett.*, 102:073005, Feb 2009.
- [27] Victor G. Ruiz, Wei Liu, Egbert Zojer, Matthias Scheffler, and Alexandre Tkatchenko. Density-Functional Theory with Screened van der Waals Interactions for the Modeling of Hybrid Inorganic-Organic Systems. *Phys. Rev. Lett.*, 108:146103, Apr 2012.
- [28] Alexandre Tkatchenko, Robert A. DiStasio, Roberto Car, and Matthias Scheffler. Accurate and Efficient Method for Many-Body van der Waals Interactions. *Phys. Rev. Lett.*, 108:236402, Jun 2012.
- [29] Material Science Group Uni Wien. The VASP Manual. URL: http://cms.mpi.univie.ac.at/wiki/index.php/The_VASP_Manual, 20.06.2018.
- [30] Alberto Ambrosetti and Anthony M. Reilly and Robert A. DiStasio Jr. and Alexandre Tkatchenko. Long-range correlation energy calculated from coupled atomic response functions. *The Journal of Chemical Physics*, 140(18):18A508, 2014.
- [31] Tomáš Bučko, Sébastien Lebègue, Tim Gould, and János Ángyán. Many-body dispersion corrections for periodic systems: an efficient reciprocal space implementation. *Journal of Physics: Condensed Matter*, 28(4):045201, 2016.
- [32] Murray Gell-Mann and Keith A. Brueckner. Correlation Energy of an Electron Gas at High Density. *Phys. Rev.*, 106:364–368, Apr 1957.
- [33] Thomas Olsen and Kristian S. Thygesen. Random phase approximation applied to solids, molecules, and graphene-metal interfaces: From van der Waals to covalent bonding. *Phys. Rev. B*, 87:075111, Feb 2013.

- [34] R. J. Maurer, V. G. Ruiz, and A. Tkatchenko. Many-body dispersion effects in the binding of adsorbates on metal surfaces. 143(10):102808, sep 2015.
- [35] G. Kresse and J. Hafner. Ab initio molecular dynamics for liquid metals. *Phys. Rev. B*, 47:558–561, Jan 1993.
- [36] G. Kresse and J. Hafner. Ab initio molecular-dynamics simulation of the liquid-metal–amorphous-semiconductor transition in germanium. *Phys. Rev. B*, 49:14251–14269, May 1994.
- [37] G. Kresse and J. Furthmüller. Efficiency of ab-initio total energy calculations for metals and semiconductors using a plane-wave basis set. *Computational Materials Science*, 6(1):15 – 50, 1996.
- [38] G. Kresse and J. Furthmüller. Efficient iterative schemes for ab initio total-energy calculations using a plane-wave basis set. *Phys. Rev. B*, 54:11169–11186, Oct 1996.
- [39] Heimel, Georg and Romaner, Lorenz and Zojer, Egbert and Brédas, Jean-Luc. A theoretical view on self-assembled monolayers in organic electronic devices. 6999, 05 2008.
- [40] Felix Bloch. Über die Quantenmechanik der Elektronen in Kristallgittern. *Zeitschrift für Physik*, 52(7):555–600, Jul 1929.
- [41] Hendrik J. Monkhorst and James D. Pack. Special points for Brillouin-zone integrations. *Phys. Rev. B*, 13:5188–5192, Jun 1976.
- [42] M. Methfessel and A. T. Paxton. High-precision sampling for Brillouin-zone integration in metals. *Phys. Rev. B*, 40:3616–3621, Aug 1989.
- [43] Neil W. Ashcroft and David N. Mermin. *Solid States Physics*. Saunders College Publishing, 1976.
- [44] J. C. Slater. Wave Functions in a Periodic Potential. *Phys. Rev.*, 51:846–851, May 1937.
- [45] O. Krogh Andersen. Linear methods in band theory. *Phys. Rev. B*, 12:3060–3083, Oct 1975.
- [46] Conyers Herring. A New Method for Calculating Wave Functions in Crystals. *Phys. Rev.*, 57:1169–1177, Jun 1940.
- [47] E. Antončík. Approximate formulation of the orthogonalized plane-wave method. *Journal of Physics and Chemistry of Solids*, 10(4):314 – 320, 1959.

- [48] James C. Phillips and Leonard Kleinman. New Method for Calculating Wave Functions in Crystals and Molecules. *Phys. Rev.*, 116:287–294, Oct 1959.
- [49] P. E. Blöchl. Projector augmented-wave method. *Phys. Rev. B*, 50:17953–17979, Dec 1994.
- [50] G. Kresse and D. Joubert. From ultrasoft pseudopotentials to the projector augmented-wave method. *Phys. Rev. B*, 59:1758–1775, Jan 1999.
- [51] A. Einstein. Über einen die Erzeugung und Verwandlung des Lichtes betreffenden heuristischen Gesichtspunkt. *Annalen der Physik*, 322:132–148, 1905.
- [52] H. Sitter, C. Draxl, and M. Ramsey. *Small Organic Molecules on Surfaces: Fundamentals and Applications*. Springer Series in Materials Science. Springer Berlin Heidelberg, 2013.
- [53] S. Weiß, D. Lüftner, T. Ules, E. M. Reinisch, H. Kaser, A. Gottwald, M. Richter, S. Soubatch, G. Koller, M. G. Ramsey, F. S. Tautz, and P. Puschnig. Exploring three-dimensional orbital imaging with energy-dependent photoemission tomography. *Nature Communications*, 6:8287–, October 2015.
- [54] Peter Puschnig, Stephen Berkebile, Alexander J. Fleming, Georg Koller, Konstantin Emtsev, Thomas Seyller, John D. Riley, Claudia Ambrosch-Draxl, Falko P. Netzer, and Michael G. Ramsey. Reconstruction of Molecular Orbital Densities from Photoemission Data. *Science*, 2009.
- [55] Peter Puschnig and Daniel Lüftner. Simulation of angle-resolved photoemission spectra by approximating the final state by a plane wave: From graphene to polycyclic aromatic hydrocarbon molecules. *Journal of Electron Spectroscopy and Related Phenomena*, 200:193 – 208, 2015. Special Anniversary Issue: Volume 200.
- [56] P. Puschnig and M.G. Ramsey. Photoemission Tomography: Valence Band Photoemission as a Quantitative Method for Investigating Molecular Films. In Klaus Wandelt, editor, *Encyclopedia of Interfacial Chemistry*, pages 380 – 391. Elsevier, Oxford, 2018.
- [57] Hannes Offenbacher, Daniel Lüftner, Thomas Ules, Eva Maria Reinisch, Georg Koller, Peter Puschnig, and Michael G. Ramsey. Orbital tomography: Molecular band maps, momentum maps and the imaging of real space orbitals of adsorbed molecules. *Journal of Electron Spectroscopy and Related Phenomena*, 204:92 – 101, 2015. Organic Electronics.

- [58] C. Seidel, R. Ellerbrake, L. Gross, and H. Fuchs. Structural transitions of perylene and coronene on silver and gold surfaces: A molecular-beam epitaxy LEED study. *Phys. Rev. B*, 64:195418, Oct 2001.
- [59] Markus Lackinger, Stefan Griessl, Wolfgang M. Heckl, and Michael Hetschold. Coronene on Ag(111) Investigated by LEED and STM in UHV. *The Journal of Physical Chemistry B*, 106(17):4482–4485, 2002.
- [60] Tobias Huempfer, Falko Sojka, Roman Forker, and Torsten Fritz. Growth of coronene on (100)- and (111)-surfaces of fcc-crystals. *Surface Science*, 639:80 – 88, 2015.
- [61] Denis Syomin, Jooho Kim, Bruce E. Koel, and G. Barney Ellison. Identification of Adsorbed Phenyl (C₆H₅) Groups on Metal Surfaces: Electron-Induced Dissociation of Benzene on Au(111). *J. Phys. Chem. B*, 105(35):8387–8394, 2001.
- [62] Jess Wellendorff, André Kelkkanen, Jens Jørgen Mortensen, Bengt I. Lundqvist, and Thomas Bligaard. RPBE-vdW Description of Benzene Adsorption on Au(111). *Topics in Catalysis*, 53(5):378–383, May 2010.
- [63] Christoph Bürker. *Adsorption geometry of π -conjugated organic molecules on metal surfaces studied with the X-ray standing wave technique*. PhD thesis, Mathematisch-Naturwissenschaftlichen Fakultät der Eberhard Karls Universität Tübingen, 2014.
- [64] Thomas Ules, Daniel Lüftner, Eva Maria Reinisch, Georg Koller, Peter Puschnig, and Michael G. Ramsey. Orbital tomography of hybridized and dispersing molecular overlayers. *Phys. Rev. B*, 90:155430, Oct 2014.
- [65] N. D. Lang and Walter Kohn. Theory of Metal Surfaces: Work Function. *Phys. Rev. B* 3, 3:1215, 1971.
- [66] Norbert Koch et. al. *The Molecule-Metal Interface*. Wiley-VCH, 2013.
- [67] Benjamin Bröker. *Electronic and structural properties of interfaces between electron donor and acceptor molecules and conductive electrodes*. PhD thesis, Humboldt-Universität zu Berlin, Mathematisch-Naturwissenschaftliche Fakultät I, 2011.
- [68] L Romaner, D Nabok, P Puschnig, E Zojer, and C Ambrosch-Draxl. Theoretical study of PTCDA adsorbed on the coinage metal surfaces, Ag(111), Au(111) and Cu(111). *New Journal of Physics*, 11(5):053010, 2009.
- [69] Bernd Kollmann. Shockley surface states calculated within density functional theory. Master Thesis. Karl-Franzens Universität, 2014.

- [70] Dario Wolf Knebl. Shockley surface states from first principles. Master Thesis, Universität Graz, 2013.
- [71] Daniel Lüftner, Simon Weiß, Xiaosheng Yang, Philipp Hurdax, Vitaliy Feyer, Alexander Gottwald, Georg Koller, Serguei Soubatch, Peter Puschnig, Michael G. Ramsey, and F. Stefan Tautz. Understanding the photoemission distribution of strongly interacting two-dimensional overlayers. *Phys. Rev. B*, 96:125402, Sep 2017.
- [72] E. Prugovecki. *Quantum Mechanics in Hilbert Space*. Academic Press, 1981.
- [73] Martijn Marsman. VASP Workshop. URL: <https://www.vasp.at/mmars/day1.pdf>, 10.05.2018.
- [74] Martin Graus. *Anwendung und Weiterentwicklung der Orbitaltomographie*. Phd thesis, Universität Würzburg, 2018.